

Weak lensing by intergalactic mini-structures in quadruple lens systems: Simulation and Detection

Ryuichi Takahashi¹ and Kaiki Taro Inoue^{2*}

¹*Faculty of Science and Technology, Hirosaki University, 3 Bunkyo-cho, Hirosaki, Aomori 036-8561, Japan*

²*Department of Science and Engineering, Kinki University, Higashi-Osaka, 577-8502, Japan*

26 July 2018

ABSTRACT

We investigate the weak lensing effects of line-of-sight structures on quadruple images in quasar-galaxy strong lens systems based on N -body and ray-tracing simulations that can resolve halos with a mass of $\sim 10^5 M_\odot$. The intervening halos and voids disturb the magnification ratios of lensed images as well as their relative positions due to lensing. The magnification ratios typically change by $O(10\%)$ when the shifts of relative angular positions of lensed images are constrained to $< 0.004''$. The constrained amplitudes of projected density perturbations due to line-of-sight structures are $O(10^8) M_\odot/\text{arcsec}^2$. These results are consistent with our new analytical estimate based on the two-point correlation of density fluctuations. The observed mid-infrared (MIR) flux ratios for 6 quasar-galaxy lens systems with quadruple images agree well with the numerically estimated values without taking into account of subhalos residing in the lensing galaxies. We find that the constrained mean amplitudes of projected density perturbations in the line-of-sight are negative, which suggests that the fluxes of lensed images are perturbed mainly by minivoids and minihalos in underdense regions. We derive a new fitting formula for estimating the probability distribution function of magnification perturbation. We also find that the mean amplitude of magnification perturbation roughly equals the standard deviation regardless of the model parameters.

Key words: cosmology: theory - gravitational lensing - dark matter - galaxies: formation

1 INTRODUCTION

In recent years, much attention has been paid to modeling of strong quasar-galaxy lensing systems with quadruple images in particular to clarifying the clustering property of dark matter at mass scales of $\lesssim 1 h^{-1} \text{Mpc}$ (Metcalf & Madau 2001; Chiba 2002). In fact, the flux ratios in some quadruply lensed quasars disagree with the prediction of best-fit lens models with a potential whose fluctuation scale is larger than the separation between the lensed images. Such a discrepancy called the ‘‘anomalous flux ratio’’ has been considered as an imprint of substructure inside a lensing galaxy (Mao & Schneider 1998; Metcalf & Madau 2001; Metcalf et al. 2004; Chiba et al. 2005; Sugai et al. 2007; McKean et al. 2007; More et al. 2009; Minezaki et al. 2009; MacLeod et al. 2009).

However, recent studies based on high resolution simulations suggested that the predicted substructure population is too low to explain the observed anomalous flux ra-

tios (Maccio & Miranda 2006; Amara et al. 2006; Xu et al. 2009, 2010; Chen 2009; Chen et al. 2011). Although detailed modeling of gravitational potential of the lens on scales comparable to or larger than the distance between the lensed images might also improve the fit (Wong et al. 2011), the origin of the anomalous flux ratios in some quadruple image systems such as B1422+231 and MG0414+0534 has been veiled in mystery (Chiba et al. 2005; Minezaki et al. 2009).

In addition to substructures in lensing galaxy, any intergalactic structures along the entire line-of-sight from the source to the observer can also perturb the flux ratios (Chen et al. 2003; Metcalf 2005; Miranda & Maccio 2007; Xu et al. 2012). Recently, taking into account of astrometric shifts, Inoue & Takahashi (2012) (hereinafter referred to as ‘‘IT12’’) has found that the observed anomaly in B1422+231 and MG0414+0534 can be explained by the line-of-sight structures without taking into account of subhalos associated with the lensing galaxies. In fact, it turned out that the observed quadruple lens systems with high redshift sources tend to exhibit more anomalous flux ratios than those with low redshift sources. As the amplitudes of convergence per-

* E-mail: kinoue@phys.kindai.ac.jp

turbation due to the line-of-sight structures increase with the source redshift, such a feature strongly supports a hypothesis that the observed flux ratio anomalies are caused by intervening structures rather than substructures associated with the primary lens.

However, IT12 used only 2-point correlation function of astrometric shifts and convergence for estimating the mean perturbation of the flux ratios. In order to evaluate the probability distribution of the perturbation, one needs to incorporate the effects of higher order correlation functions as well. Furthermore, it is of great importance to determine the role of underdense regions (voids). On the one hand, the effect of each perturbation by an underdense region (void) is expected to be smaller than that by an overdense region (halo) since the maximum amplitude of the former is much smaller than that of the latter. On the other hand, the probability of perturbation by underdense regions is much larger than that by overdense regions since the total volume of underdense regions is much larger. Thus, the overall effect is non-trivial. To probe such non-linear effects, one needs to perform ray-tracing simulations using particle distributions obtained from N -body simulations.

In this paper, we numerically explore the non-linear effects in weak lensing due to line-of-sight structures in quasar-galaxy quadruple lensing systems. In what follows, we assume a cosmology with a matter density $\Omega_m = 0.272$, a baryon density $\Omega_b = 0.046$, a cosmological constant $\Omega_\Lambda = 0.728$, the Hubble constant $H_0 = 70$, km/s/Mpc, the spectrum index $n_s = 0.97$, and the root-mean-square (rms) amplitude of matter fluctuations at $8h^{-1}$ Mpc, $\sigma_8 = 0.81$, which are obtained from the observed CMB (WMAP 7yr result, (Jarosik et al. 2011)), the baryon acoustic oscillations (Percival et al. 2010), and H_0 (Riess et al. 2009).

2 WEAK LENSING EFFECTS OF LINE-OF-SIGHT STRUCTURES ON MAGNIFICATIONS OF MULTIPLE IMAGES

In this section, we introduce the weak lensing effects due to intervening halos and voids in quasar-galaxy lens systems. First, we discuss simple primary lens systems and then we treat the lensing effects of line-of-sight structures as perturbations to the primary lens. Our objective is to derive the magnification perturbation of each lensed image induced by intervening structures.

When a light ray from a distant quasar passes in the neighborhood of a massive lensing galaxy (primary lens), multiple images of the quasar are formed due to deflection of light. The source position β and the image position θ are related via the lens equation (e.g. Schneider et al. 1992),

$$\beta = \theta - \frac{D_{LS}}{D_S} \hat{\alpha}_L(\theta), \quad (1)$$

where $\hat{\alpha}_L$ is the deflection angle by the primary lens, and $D_{LS}(D_S)$ is the angular-diameter distance from the lens (observer) to the source. The image positions are obtained as solutions of the lens equation (1). In what follows, we use a suffix i for labeling each image ($i = 1, 2, \dots$). The image deformation is characterized by the Jacobian matrix,

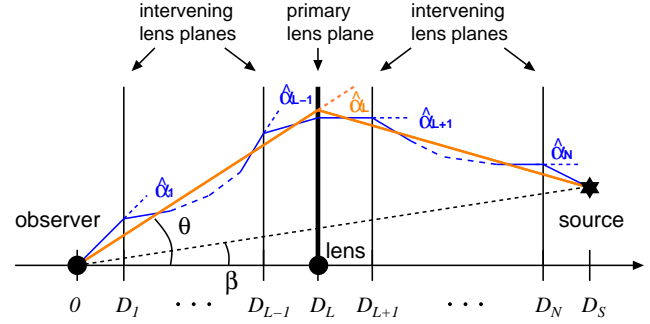


Figure 1. A configuration of multiple lens system. In the horizontal axis, D_j with $j = 1, 2, \dots, N$ is the angular diameter distance from the observer to the j -th lens plane, and here $j = L$ corresponds to the primary lens. θ and β are the angular positions of the image and the source. The blue line shows the light-ray path in the multiple scattering. The light-ray is deflected at each lens plane by the angle $\hat{\alpha}_j$ on the j -th lens plane. The orange lines are the unperturbed light-ray paths in which we ignore the deflection by the intervening lens planes.

$A_L = \partial\beta/\partial\theta$. For the i -th image, the matrix is

$$A_{L,i} = \begin{pmatrix} 1 - \kappa_i - \gamma_{i1} & -\gamma_{i2} \\ -\gamma_{i2} & 1 - \kappa_i + \gamma_{i1} \end{pmatrix}, \quad (2)$$

where κ_i and $\gamma_{i1,2}$ are the convergence and the shear of the i -th image whose angular sizes are sufficiently small. The magnification is $\mu_i = 1/\det(A_{L,i}) = 1/[(1 - \kappa_i)^2 - \gamma_i^2]$ where $\gamma_i^2 = \gamma_{i1}^2 + \gamma_{i2}^2$. The images are classified into three types: minimum, saddle, and maximum according to the curvature tensor of the arrival time surface at a lensed image (or the Fermat potential; e.g. Schneider et al. 1992). Type I is a minimum image such that $\gamma < 1 - \kappa \leq 1$, type II is a saddle image, $(1 - \kappa)^2 < \gamma^2$, and type III is a maximum image, $(1 - \kappa)^2 > \gamma^2$ and $\kappa > 1$.

Next, we consider multiple lens planes between the observer and the source. The configuration of multiple lensing is shown in Fig. 1. N lens planes are located at the angular-diameter distance D_j ($j = 1, 2, \dots, N$), where $j = L$ corresponds to the primary lens while the others ($j \neq L$) correspond to the intervening lenses. The blue line indicates the light-ray path in the multiple scattering. In multiple lens planes, the lens equation is given by,

$$\beta = \theta_1 - \frac{D_{LS}}{D_S} \hat{\alpha}_L(\theta_L) - \sum_{j \neq L} \frac{D_{jS}}{D_S} \hat{\alpha}_j(\theta_j) \quad (3)$$

where θ_j and $\hat{\alpha}_j$ denote the light-ray position and the deflection angle on the j -th lens plane, respectively and D_{jS} is the angular-diameter distance from the j -th lens plane to the source. In the following, we assume that the deflection angles caused by intervening structures are much smaller than that by the primary lens. Then we can ignore the last term in equation (3). This assumption corresponds to the Born approximation. The orange lines in Fig. 1 are unperturbed light-ray paths under the assumption of the Born approximation. From equation (1), the position of an unperturbed

light-ray on the j -th plane is given by,

$$\begin{aligned}\boldsymbol{\theta}_j &= \boldsymbol{\theta}_1, \quad \text{for } j \leq L \\ &= \boldsymbol{\theta}_1 - \frac{D_{Lj}}{D_j} \hat{\boldsymbol{\alpha}}_L(\boldsymbol{\theta}_1), \quad \text{for } j > L\end{aligned}\quad (4)$$

where D_{Lj} is the angular diameter distance between the primary lens plane and the j -th lens plane. From equation (3), the magnification matrix, $A = \partial\boldsymbol{\beta}/\partial\boldsymbol{\theta}_1$, is given by

$$A = A_L + \delta A, \quad \delta A = - \sum_{j \neq L} \frac{D_{jS}}{D_S} \frac{\partial \hat{\boldsymbol{\alpha}}_j(\boldsymbol{\theta}_j)}{\partial \boldsymbol{\theta}_1}. \quad (5)$$

Note that the derivative in δA is calculated along the unperturbed path. Then, the magnification matrix for the i -th image is,

$$\begin{aligned}A_i &= A_{L,i} + \delta A_i = \begin{pmatrix} 1 - \kappa_i - \gamma_{i1} & -\gamma_{i2} \\ -\gamma_{i2} & 1 - \kappa_i + \gamma_{i1} \end{pmatrix} \\ &+ \begin{pmatrix} -\delta\kappa_i - \delta\gamma_{i1} & -\delta\gamma_{i2} \\ -\delta\gamma_{i2} & -\delta\kappa_i + \delta\gamma_{i1} \end{pmatrix}.\end{aligned}\quad (6)$$

The second matrix is the correction term due to intervening structures. The total magnification is $\mu_i + \delta\mu_i = 1/\det(A_{L,i} + \delta A_i)$. The fractional difference of the magnification for the i -th image

$$\delta_i^\mu \equiv \frac{\delta\mu_i}{\mu_i}, \quad (7)$$

is approximately given by

$$\delta_i^\mu \simeq 2 \frac{(1 - \kappa_i) \delta\kappa_i + \gamma_{1i} \delta\gamma_{1i} + \gamma_{2i} \delta\gamma_{2i}}{(1 - \kappa_i^2)^2 - \gamma_i^2}, \quad (8)$$

up to first order in $\delta\kappa$, $\delta\gamma_{1,2}$ and $\delta\mu$. We numerically evaluate the perturbations using the ray-tracing simulation.

We use a statistic η introduced by IT12 to measure the magnification perturbation of lensed images in quasar-galaxy lens systems:

$$\eta \equiv \left[\frac{1}{2N_{\text{pair}}} \sum_{i \neq j} [\delta_i^\mu(\text{minimum}) - \delta_j^\mu(\text{saddle})]^2 \right]^{1/2} \quad (9)$$

where $\delta^\mu(\text{minimum})$ and $\delta^\mu(\text{saddle})$ are the magnification perturbations given in equation (7) corresponding to the minimum and saddle images. Roughly speaking, η is equal to the magnification contrast averaged over the lensed images if correlation of flux perturbation between the lensed images are negligible. The summation is performed over all the pairs of the minimum and the saddle images, and N_{pair} is the total number of the pairs. For three images of two minima A, C, and a saddle B, we have

$$\eta = \frac{1}{2} \left[(\delta_A^\mu - \delta_B^\mu)^2 + (\delta_C^\mu - \delta_B^\mu)^2 \right]^{1/2}. \quad (10)$$

Similarly, for four images of two minima A, C and two saddles B, D, we have

$$\begin{aligned}\eta &= \frac{1}{\sqrt{8}} \left[(\delta_A^\mu - \delta_B^\mu)^2 + (\delta_C^\mu - \delta_B^\mu)^2 \right. \\ &\quad \left. + (\delta_A^\mu - \delta_D^\mu)^2 + (\delta_C^\mu - \delta_D^\mu)^2 \right]^{1/2}.\end{aligned}\quad (11)$$

To measure η , we first need to estimate the unperturbed fluxes f_i^0 based on the best-fit lens model (see sec.5.1 for detail) and observed fluxes f_i for each i -th image. Therefore, η is a model dependent quantity. Then, we can estimate the

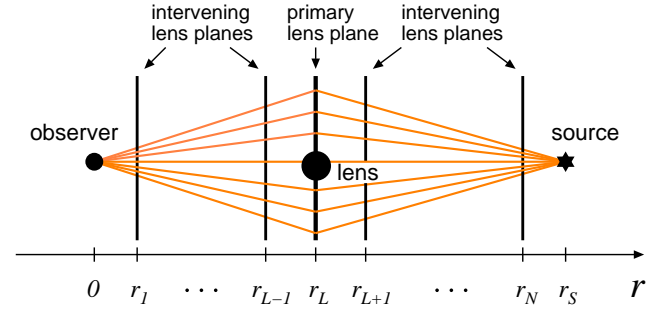


Figure 2. A schematic picture of our ray-tracing simulation. The horizontal axis is the comoving distance r from the observer. The vertical thick lines denote the positions of the lens planes at $r_j = L_{\text{box}} \times (j - 1/2)$ with $j = 1, 2, \dots, L, \dots, N$. The primary lens plane is located at $j = L$, and the others correspond to intervening lens planes. The source plane is placed at $r_s = L_{\text{box}} \times N$. Here, we set $L_{\text{box}} = 10h^{-1}\text{Mpc}$. The orange lines are unperturbed light rays from the source to the observer. We consider 1000^2 light rays that converge at the observer within the field-of-view of 38.4^2arcsec^2 .

magnification contrast $\delta_i^\mu = (f_i - f_i^0)/f_i^0$ and also η using the above equations.

3 RAY-TRACING SIMULATIONS

We carry out ray-tracing simulations to calculate the perturbed convergence, shear and deflection angle due to intervening structures. Fig. 2 shows a schematic picture of our ray-tracing simulation. The horizontal axis denotes the comoving distance r from the observer: The thick vertical line is the primary lens plane, and the thin vertical lines correspond to the intervening lens planes. The lens planes are placed at an equal distance interval of L_{box} , $r_j = L_{\text{box}} \times (j - 1/2)$ with an integer $j = 1, 2, \dots, L, \dots, N$. Here, $j = L$ corresponds to the primary lens plane. The source plane is placed at $r_s = L_{\text{box}} \times N$. The interval of the lens planes is set to $L_{\text{box}} = 10h^{-1}\text{Mpc}$. We prepare 520 lens planes up to the source redshift $z_s = 4$. The orange lines are light-ray paths from the source to the observer, which are deflected at the primary lens plane. We use the Born approximation in which the lensing quantities such as the convergence, shear, deflection angle are evaluated along unperturbed paths.

3.1 N -body simulations

We run N -body simulations on a cubic box with sides L_{box} , and then project the positions of particles to a plane at each redshift bin, and obtain the particle distribution and gravitational potentials on intervening lens planes by considering randomly oriented observers at each redshift bin. Note that the effects of large-scale correlation between different snapshots are suppressed due to the randomisation of orientation. As long as we concern with structures whose sizes are much less than the size of the cubic box, such effects are negligible. We use the numerical N -body simulation code Gadget2

(Springel et al. 2001; Springel 2005). The initial conditions of our simulations are calculated using the second-order Lagrangian perturbation theory (2LPT) (Crocco et al. 2006; Nishimichi et al. 2009) with an initial linear power spectrum (Eisenstein & Hu 1999). We dump the outputs (the particle positions) at the redshifts that correspond to the positions of lens planes $r_j = L_{\text{box}} \times (j - 1/2)$, as shown in Fig. 2.

We run a high and a low resolution simulations to check our numerical convergence at small scales. In the high (low) resolution simulation, we employ 1024^3 (512^3) dark matter particles on a simulation box with the sides of $L_{\text{box}} = 10h^{-1}$ Mpc and the softening length is set to 2% of the mean particle separations for the both cases. The particle mass is 7.1×10^4 (5.7×10^5) $h^{-1} M_{\odot}$ for high (low) resolution case. We prepare a single realisation (two realisations) for the high (low) resolution simulation. The simulation data are the same as that used in our previous paper (IT12). The matter power spectra of our N -body simulations agree with the results of the simulation with higher resolution in which we use finer simulation parameters for the time step, force calculation, etc., within 2(6)% for $k < 100(320)h\text{Mpc}^{-1}$.

Before closing this section, we comment on the effects of our smaller simulation box on our results. Our simulation box is very small ($L_{\text{box}} = 10h^{-1}\text{Mpc}$ on a side) and hence it does not include the larger fluctuations than the box size which may affect the small-scale clustering and even worse the whole box may enters in the non-linear regime. However, our simulation results can be trusted because of the following reasons: i) As shown in Fig.2 in our previous paper (IT12), the computed matter power spectra for a larger box ($L_{\text{box}} = 320h^{-1}\text{Mpc}$) can be smoothly connected to the power spectra for the small one ($L = 10h^{-1}\text{Mpc}$) at $k \sim 30h\text{Mpc}^{-1}$ for redshifts $z = 0 - 2.2$. This suggests that our simulations successfully reproduce the clustering of dark matter at smaller scales $< 200h^{-1}\text{pc}$ ($k/30h\text{Mpc}^{-1}$)⁻¹. ii) To check the non-linearity in the whole simulation box, we evaluate the mass variance in the box analytically¹. The standard deviations are $\sigma_{\text{box}} = 0.39, 0.30, 0.23$ and 0.15 at redshifts $z = 0, 0.5, 1$ and 2 . Note that the most important intervening structures reside at relatively higher redshifts $z \gtrsim 0.5$, and hence the variance is smaller than unity. This suggests that the simulated particles in the small box are in the linear regime.

3.2 Ray-tracing simulations

We briefly explain our procedure to trace light rays through the obtained N -body data. We use a publicly available code called RAYTRIX (Hamana & Mellier 2001) which follows the standard multiple lens plane algorithm². The distance

¹ The mass variance within the cubic box of size L is given by,

$$\sigma_{\text{box}}^2(z; L) = \int \frac{d^3k}{(2\pi)^3} |\tilde{W}(\mathbf{k}; L)|^2 P_{\delta}(k, z), \quad (12)$$

where we use the top-hat window function of the cubic box as, $W(\mathbf{x}; L) = 1/L^3$ for $|x| < L/2, |y| < L/2$ and $|z| < L/2$, and $W = 0$ otherwise. \tilde{W} is its Fourier component given by $\tilde{W}(\mathbf{k}; L) = \text{sinc}(k_x L/2) \text{sinc}(k_y L/2) \text{sinc}(k_z L/2)$ with $\text{sinc}(x) = \sin(x)/x$. For the matter power spectrum $P_{\delta}(k, z)$, we use the non-linear fitting formula given in IT12.

² see <http://th.nao.ac.jp/MEMBER/hamanatk/RAYTRIX/>

between an observer and a source is divided into a lot of intervals. As shown in Fig. 2, we adopt a fixed interval of L_{box} . Particle positions are projected onto two dimensional lens planes (xy, yz, zx planes) at every interval L_{box} on each light ray path. Using the Triangular-Shaped Cloud (TSC) method (Hockney & Eastwood 1988), we assign the particles onto N_g^2 grids in the lens planes, then compute the projected density contrast at each plane. We test the convergence of our simulations by varying resolution as $N_g^2 = 2048^2, 4096^2, 8192^2$ and 16384^2 which correspond to the grid sizes $r_{\text{grid}} \equiv L_{\text{box}}/N_g = 4.8, 2.4, 1.2$ and $0.6 h^{-1}\text{kpc}$, respectively. The two-dimensional gravitational potential is solved via the Poisson equation using Fast Fourier Transform. Finally, the two dimensional sky maps of the convergence, shear, and deflection angle of light rays are obtained by solving the evolution equation of the Jacobian matrix along the unperturbed light-ray paths.

We prepare 100 realisations for each lens system by randomly choosing the projected direction and shifting the two dimensional projected positions. In each realisation, we emit 1000^2 light-rays in the field of view of $38.4 \times 38.4 \text{ arcsec}^2$, and the resulting angular resolution is 0.04 arcsec .

Before closing this section, we comment on our simplifications for implementing fast-calculation. First, instead of changing the position of a source, we change the position of the center of a lens (there are 1000^2 points in single realisation) as shown in panel (a) of Fig. 3. In panels (a1) and (a2), a lens system (which consists of a lens and double images at angular separations $\theta_{1,2}$ from the lens center) is put on different points on the primary lens plane. As long as the angular separation between lensed images is much smaller than the distance from the observer to the source, the statistics of the perturbed convergence and shear do not depend on the position of the lens because of the spatial homogeneity of the perturbations. In order to reduce the calculation time, we choose all the grid points as the lens centers for each realisation in calculating the probability distribution function of magnification perturbation.

Next, in order to reduce the computation time, we use only photon paths that have a ‘‘diamond shape’’ centered at the lens center as shown in orange lines in Fig. 2. In a real setting, however, light rays passing sufficiently close to the lens intersect each other before reaching backward to the source (as shown by the dotted lines in Fig. 3), whereas the light rays passing far from the lens does not converge completely at the source plane (the dashed lines in Fig. 3). The light-ray paths as shown in Fig. 2 are correct only for a circular symmetric lens where the source is put at the lens center. Any deviation from this setting cause errors in calculating statistical quantities.

4 MIR QUADRUPLE LENSES

In this paper, we use the observed MIR (mid-infrared) flux ratios in six lens systems: B1422+231, MG0414+0534, H1413+117, PG1115+080, Q2237+030 and RXJ1131-1231. We use the observed flux of [OIII] line for RXJ1131-1231, and those of continuum for the other systems. Table 1 summarises the observed data: in the first column, we list the names of lens systems with the source and lens redshifts, in the second column, the names of images (A,B,C,...) with

Table 1. MIR lens systems

lens system	image(type)	position(arcsec)	flux ratio(obs.)	κ	γ_1	γ_2	μ	flux ratio(model)
B1422+231 $z_L = 0.34$ $z_S = 3.62$	A(I)	$(-0.385 \pm 0.000, 0.317 \pm 0.000)$	A/B= 0.94 ± 0.05	0.384	0.251	-0.408	6.669	A/B=0.797
	B(II)	(0., 0.)		0.469	-0.098	-0.626	-8.370	
	C(I)	$(0.336 \pm 0.003, -0.750 \pm 0.003)$	C/B= 0.57 ± 0.06	0.364	-0.401	-0.099	4.293	C/B=0.513
	D(II)	$(-0.948 \pm 0.004, -0.802 \pm 0.003)$		1.859	-0.705	1.897	-0.298	
	G	$(-0.742 \pm 0.003, -0.656 \pm 0.004)$						
MG0414+0534 $z_L = 0.96$ $z_S = 2.639$	A1(I)	$(-0.600 \pm 0.003, -1.942 \pm 0.003)$		0.509	-0.228	-0.360	16.593	
	A2(II)	$(-0.732 \pm 0.003, -1.549 \pm 0.003)$	A2/A1= 0.919 ± 0.021	0.548	-0.486	-0.161	-17.233	A2/A1=1.039
	B(I)	(0., 0.)	B/A1= 0.347 ± 0.013	0.464	0.145	0.288	5.456	B/A1=0.329
	C(II)	$(1.342 \pm 0.003, -1.650 \pm 0.003)$		0.660	-0.409	0.564	-2.704	
	G	$(0.472 \pm 0.003, -1.277 \pm 0.003)$						
H1413+117 $z_L = 1.88(\star)$ $z_S = 2.55$	X	$(0.857 \pm 0.011, 0.180 \pm 0.009)$						
	A(II)	(0., 0.)		0.568	0.437	-0.388	-6.430	
	B(I)	$(-0.744 \pm 0.003, 0.168 \pm 0.003)$	B/A= 0.84 ± 0.07	0.481	-0.101	0.288	5.748	B/A=0.894
	C(I)	$(0.492 \pm 0.003, 0.713 \pm 0.003)$	C/A= 0.72 ± 0.07	0.458	-0.347	0.045	5.820	C/A=0.905
	D(II)	$(-0.354 \pm 0.003, 1.040 \pm 0.003)$	D/A= 0.40 ± 0.06	0.654	0.454	-0.503	-2.948	D/A=0.458
PG1115+080 $z_L = 0.31$ $z_S = 1.72$	G	$(-0.142 \pm 0.003, 0.561 \pm 0.003)$						
	X	$(-1.87 \pm 0.07, 4.14 \pm 0.07)$						
	A1(I)	$(-1.328 \pm 0.003, -2.034 \pm 0.003)$		0.502	-0.188	0.369	13.099	
	A2(II)	$(-1.477 \pm 0.004, -1.576 \pm 0.003)$	A2/A1= 0.93 ± 0.06	0.546	-0.526	0.113	-11.950	A2/A1=0.912
	B(II)	$(0.341 \pm 0.003, -1.961 \pm 0.003)$		0.602	-0.101	-0.704	-2.87438	
Q2237+030 $z_L = 0.04$ $z_S = 1.695$	C(I)	(0., 0.)		0.387	0.309	0.088	3.66826	
	G	$(-0.381 \pm 0.003, -1.344 \pm 0.003)$						
	A(I)	(0., 0.)		0.394	0.388	0.078	4.733	
	B(I)	$(0.673 \pm 0.003, 1.697 \pm 0.003)$	B/A= 0.84 ± 0.05	0.375	0.086	0.380	4.197	B/A=0.887
	C(II)	$(-0.635 \pm 0.003, 1.210 \pm 0.003)$	C/A= 0.46 ± 0.02	0.743	-0.555	-0.480	-2.117	C/A=0.447
RXJ1131-1231(**) $z_L = 0.295$ $z_S = 0.658$	D(II)	$(0.866 \pm 0.003, 0.528 \pm 0.003)$	D/A= 0.87 ± 0.05	0.636	-0.367	-0.504	-3.904	D/A=0.825
	G	$(0.075 \pm 0.004, 0.939 \pm 0.003)$						
	A(II)	$(-0.588 \pm 0.003, 1.120 \pm 0.003)$	A/B= $1.63^{+0.04}_{-0.02}$	0.464	-0.512	0.274	-20.276	A/B=1.657
	B(I)	$(-0.618 \pm 0.003, 2.307 \pm 0.003)$		0.420	-0.465	-0.196	12.239	
	C(I)	(0., 0.)	C/B= $1.19^{+0.03}_{-0.12}$	0.441	-0.049	0.470	11.124	C/B=0.909
RXJ1131-1231(**)	D(II)	$(2.517 \pm 0.003, 1.998 \pm 0.003)$		0.886	-0.862	0.510	-1.011	
	G	$(1.444 \pm 0.008, 1.706 \pm 0.006)$						

Note: (\star): The lens redshift z_L is obtained from a best-fit model using the observed positions of the images and the primary lens, the flux ratios, and the time-delays between the images assuming $H_0 = 70$ km/s/Mpc. (**): [OIII] line flux ratios.

the types (I,II) and lens (G), in the third column, the angular positions of lensed images and the centroid of each lensing galaxy in terms of right ascension and declination (in units of arcsec), in the fourth column, the MIR flux ratios. The data of positions of lensed images and centroids of lensing galaxies are taken from the CASTLES webpage³ (note that the signs of right ascension in the Table 1 are opposite to those in the CASTLES webpage). The six lens systems are listed in descending order of the source redshift.

The MIR bands are suitable to probe intervening structures with mass scales of $\gtrsim 10^3 M_\odot$ assuming that the size of a MIR emission region around a quasar is ~ 1 pc. This is because the Einstein radii of a point mass with a mass $\sim 10^3 M_\odot$ are ~ 1 pc at cosmological distances. On the other hand, the Einstein radius of stars residing at a lensing galaxy is typically ~ 0.001 pc. Therefore, microlensing effect due to stars is negligible provided that the filamentary structure

of hot dust torus is not prominent (Stalevski et al. 2012) (see also Sluse et al. (2013)). Moreover, the dust extinction is very small in the MIR bands. Hence, the MIR flux ratios provide us variable information about structures in the line-of-sight or lensing galaxies (e.g. Chiba et al. 2005).

In the following, we shortly describe observed quantities for each lens. For detail, see IT12.

The cusp-caustic lens B1422+231 consists of three bright images A, B, C, and a faint image D. Images A, C are minima and B, D are saddles. It was first discovered by Patnaik et al. (1992) using the Very Large Array. The quasar redshift is $z_S = 3.62$ and the lensing galaxy is at $z_L = 0.34$ (Kundic et al. 1997; Tonry 1998). The MIR image fluxes were measured by Chiba et al. (2005) using the Subaru telescope. We use the flux ratios using the bright images A, B, and C (A/B and C/B). When the source is close to and inside a cusp, then the bright images A, B, C can form and the flux ratios satisfy the so called cusp caustic relation: $R = (\mu_A + \mu_B + \mu_C) / (|\mu_A| + |\mu_B| + |\mu_C|) = 0$. However, the relation does not hold in the optical, MIR, and radio bands.

³ <http://www.cfa.harvard.edu/castles/>

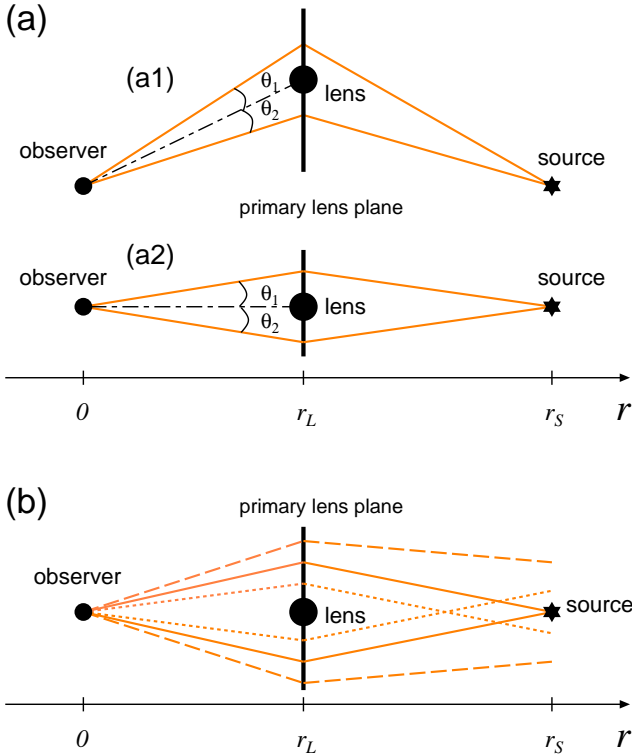


Figure 3. Same as Fig. 2, but show two lens systems in panel (a) and “exact” light-rays in panel (b). In panel (a), a lens system (which consists of a lens and two images) is put on two different positions on the primary lens plane, denoted as (a1) and (a2). The relative image positions θ_1 and θ_2 as measured from the lens center for (a1) are the same as those for (a2), respectively. In panel (b), the orange solid lines are the light-rays that converge at the position of the observer. The dotted (dashed) lines are the light-rays that are closer to (far from) the lens at the lens plane.

The observed flux ratios show an anomaly $R \simeq 0.2$ in the MIR (Chiba et al. 2005) and the radio (Mao & Schneider 1998) bands.

The fold-caustic lens MG0414+0534 consists of two bright images A1, A2 and two faint images B, C. The images A1, B are minima and A2, C are saddles. A source quasar at $z_S = 2.64$ is lensed by an elliptical galaxy at $z_L = 0.96$ (Hewitt et al. 1992; Lawrence et al. 1995; Tonry & Kochanek 1999). A simple lens model, a singular isothermal ellipsoid with an external shear (SIE-ES) can not fit the image positions as well as the flux ratios. Schechter & Moore (1993) and Ros et al. (2000) suggested that another galaxy called “X” is necessary to account for the relative image positions. Minezaki et al. (2009) measured the MIR flux ratios using the Subaru telescope. Recently, MacLeod et al. (2012) have provided more accurate MIR flux ratios using the Gemini(north) telescope. The observed flux ratios show an anomaly $R \simeq 0.2$ in the MIR (Minezaki et al. 2009; MacLeod et al. 2012) and the radio (Ros et al. 2000; Trotter et al. 2000) bands. We use the MIR flux ratios among the bright images A1, A2 and B

(A2/A1 and B/A1) measured by Minezaki et al. (2009) and MacLeod et al. (2012).

The clover leaf lens H1413+117 consists of four bright images A, B, C and D. The images B, C are minima and A, D are saddles. The source redshift is $z_S = 2.55$ (Magain et al. 1988) but the lens redshift is unknown. Goicoechea & Shalyapin (2010) measured the time delays among the images A-D and estimated the lens redshift, $z_L = 1.88^{+0.09}_{-0.11}$. MacLeod et al. (2009) modeled a galaxy “X” as a singular isothermal sphere (SIS) to improve the fitting of the image positions and the flux ratios. We use the MIR flux ratios among the four images A,B,C and D (B/A, C/A and D/A) measured by MacLeod et al. (2009).

The fold-caustic lens PG1115+080 consists of two bright images A1, A2 and two faint images C, D. A source quasar at $z_S = 1.72$ is lensed by a foreground galaxy at $z_L = 0.31$ (Weymann et al. 1980; Kundic et al. 1997). We use the MIR flux ratios between A1 (minimum) and A2 (saddle) measured by Chiba et al. (2005).

The clover leaf lens Q2237+030 is the nearest lens in our samples and it consists of four images A, B, C, and D. The images A, B are minima and C, D are saddles. The source is located at $z_S = 1.695$ and the lens at $z_L = 0.0394$ (Huchra et al. 1985). We use the flux ratios among the four images A, B, C, and D (B/A, C/A and D/A) measured by Minezaki et al. (2009).

The cusp-caustic lens RXJ1131-1231 consists of three bright images A, B, C, and a faint image D. The quasar at $z_S = 1.72$ lensed by a foreground galaxy at $z_L = 0.31$ (Sluse et al. 2003). We use the [OIII] flux ratios of images A (saddle), B (minimum) and C (minimum) (A/B and C/B) measured by Sugai et al. (2007).

5 METHOD

This section describes our procedure for evaluating the weak lensing effects caused by the line-of-sight structures on the flux ratios of lensed images. First, we make a primary lens model to fit the observed MIR image positions, and then we evaluate the unperturbed convergence κ_i and shear γ_i for each image. Next, we obtain the perturbed convergence $\delta\kappa_i$ and shear $\delta\gamma_i$ due to the line-of-sight structures using ray-tracing simulations, and then we add the perturbed quantities $\delta\kappa_i, \delta\gamma_i$ to the original ones κ_i, γ_i . Finally, we evaluate the magnification contrast $\delta\mu_i^m = \delta\mu_i/\mu_i$ and the magnification perturbation η defined in equation (9).

5.1 Primary lens model

First, for each lens system, we fit the observed positions of lensed images and the centroid of a lensing galaxy by changing the lens parameters of a smooth mass lens model. Note that we do not include the measured MIR fluxes in the fitting. For detailed discussion, see IT12. We use a singular isothermal ellipsoid (SIE) with an external shear (ES) (e.g., Schneider et al. 2006) as a canonical lens model. The SIE model is characterized by the effective Einstein radius b' , position of the lens center θ_0 , and ellipticity e with the position angle θ_e . The external shear is expressed in terms of the amplitude γ and the direction ϕ_γ . In terms of these parameters, the lensing potential of a SIE plus ES (SIE-ES)

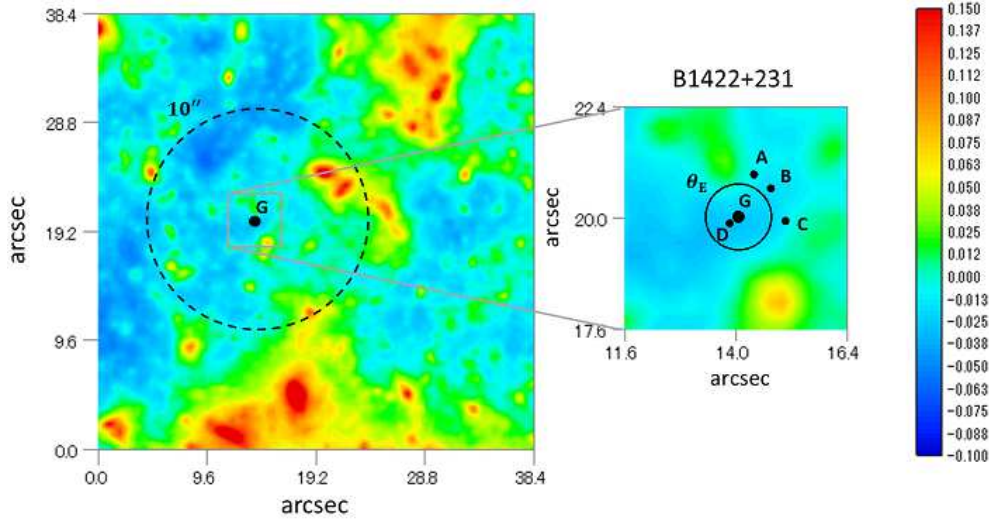


Figure 4. Contour map of convergence perturbation $\delta\kappa$ due to the line-of-sight structures for B1422+231. The contours in the left panel show the total field of view of $38.4 \times 38.4 \text{sec}^2$, and those in the right panel show the enlarged view around a lens. The point G is the centroid of the lensing galaxy and A, B, C, and D correspond to the image positions. In the left panel, a dashed circle centered at G has a radius of 10 arcsec. Similarly, in the right panel, the circle has an effective Einstein radius of the lens. The map is obtained from a simulation of 1024^3 N -body particles with a grid radius $r_{\text{grid}} = 1.2h^{-1} \text{kpc}$.

Table 2. Best-fit model parameters for 6 MIR lens systems (see IT12 for detail)

lens system	b' (arcsec)	b_X (arcsec)	θ_0 (arcsec)	e	θ_e (deg)	γ	θ_γ (deg)
B1422+231	0.755		(-0.741, -0.658)	0.309	-56.6	0.166	-52.3
MG0414+0534	1.08	0.185	(0.472, -1.277)	0.232	-82.1	0.102	53.8
H1413+117	0.561	0.583	(-0.172, 0.561)	0.204	-14.5	0.062	55.7
PG1115+080	1.14		(-0.361, -1.342)	0.156	-83.0	0.110	51.8
Q2237+030	0.854		(0.075, 0.939)	0.371	64.9	0.015	-46.8
RXJ1131-1231	1.83		(2.039, 0.568)	0.145	-57.8	0.120	-81.8

can be written as

$$\phi(\boldsymbol{\theta}) = \tilde{\boldsymbol{\theta}} \cdot \boldsymbol{\alpha}(\tilde{\boldsymbol{\theta}}) - \frac{\theta^2}{2} \gamma \cos[2(\phi_\theta - \phi_\gamma)], \quad (13)$$

where $\boldsymbol{\theta} = (\theta_1, \theta_2) = (\theta \cos \phi_\theta, \theta \sin \phi_\theta)$ is the angular coordinate from the lens center $\boldsymbol{\theta}_0$, and $\tilde{\boldsymbol{\theta}}$ is the coordinate rotated by an angle θ_e : $\tilde{\theta}_1 = \theta_1 \cos \theta_e + \theta_2 \sin \theta_e$, $\tilde{\theta}_2 = -\theta_1 \sin \theta_e + \theta_2 \cos \theta_e$. The deflection angle $\boldsymbol{\alpha}(\boldsymbol{\theta})$ of the SIE is given by,

$$\alpha_{1,2}(\tilde{\boldsymbol{\theta}}) = \frac{b'q}{\sqrt{1-q^2}} \tan^{-1} \left[\frac{\sqrt{1-q^2}}{\sqrt{q^2 \tilde{\theta}_1^2 + \tilde{\theta}_2^2}} \tilde{\theta}_{1,2} \right]. \quad (14)$$

where $q = 1 - e$. We use the public code GRAVLENS⁴ by Keeton to find the best-fit model parameters. Note again that we use only the positions of lensed images and the centroid of the primary lens to fit the model parameters. The

best-fit parameters for all the systems are summarised in Table 2. The resulting convergence κ_i , shear γ_i , magnification μ_i for each image based on the best fitting model are shown in Table 1 (from the 5th to 8th columns). Similarly, the theoretically predicted flux ratios are shown in the last column in Table 1. For MG0414 and H1413, object ‘‘X’’, modeled by a singular isothermal sphere, is added at the positions (0.857, 0.180) and (-1.87, 4.14) arcsec, respectively. The effective Einstein radii b_X are shown in Table 1. For detail, see IT12.

5.2 Weak lensing by line-of-sight structures

As discussed in section 3, we prepare 100 lensing convergence and shear maps for each lens system using our ray-tracing simulations. The field of view is $38.4 \times 38.4 \text{sec}^2$ with 1000^2 grids, and thus the resulting angular resolution is 0.038 arcsec. In Fig. 4, we plot an example of the convergence perturbation due to the line-of-sight structures for B1422+231. The left panel and the right panel indicate the total field of

⁴ <http://redfive.rutgers.edu/~keeton/gravlens/>

view of $38.4 \times 38.4 \text{sec}^2$ and the enlarged view around the primary lens, respectively. The centroid of the lensing galaxy is denoted as G and the image positions are A, B, C, and D. In the maps, red spots correspond to overdense regions, while blue spots to underdense regions (or voids). We can see some massive clumps or filamentary structures in the neighborhood of the primary lens. We obtain the perturbed convergence $\delta\kappa_i$ and shear $\delta\gamma_{i,1,2}$ on grid points at image positions.

In what follows, we describe our procedure for evaluating the probability distribution of magnification perturbation.

1) We put the lens center at an arbitrary grid point in a simulated map and also put the images of a point source on the observed image positions. In this procedure, we do not allow to place a halo that is more massive than the primary lens in the line-of-sight since it should be “primary”. As a result, we impose the following two conditions in our analysis: (i) Convergence perturbations in a $10''$ circle around the primary lens galaxy is less than 0.5. The circle is plotted as dashed curve in Fig. 4. (ii) Convergence perturbations $\delta\kappa$ and shear perturbations $\delta\gamma$ should be smaller than those of the primary lens, i.e. $|\delta\bar{\kappa}| < |\bar{\kappa}|$ and $|\delta\bar{\gamma}| < |\bar{\gamma}|$. Here, $\delta\bar{\kappa}$ and $\delta\bar{\gamma}$ are the mean perturbed convergence and shear inside a circle with the Einstein radius at the lens center, and $\bar{\kappa}$ and $\bar{\gamma}$ are the mean convergence and shear among all the images in the lens system.

In our analysis, we include only samples that satisfy the above two conditions. Note that almost all the light rays satisfy the above conditions (i) and (ii). The convergence and shear perturbations are usually much smaller than 1. For instance, only 3%(0.2%) rays have $\delta\kappa > 0.1(0.3)$ in B1422+231. Since the source redshift of B1422+231 is the highest in the six lens systems, the convergence perturbations $\delta\kappa$ in the other systems are naturally smaller than that in B1422+231.

2) We obtain the convergence perturbations $\delta\kappa_i$ and shear perturbations $\delta\gamma_i$ for the macro-lensed images from our ray-tracing simulation. However, contribution from the external shear and the constant convergence is already taken into account in the primary lens. Therefore, we should subtract the mean shear and convergence perturbations around the lens in order to avoid the double-counting. We calculate the mean convergence and shear perturbations, $\delta\bar{\kappa}$ and $\delta\bar{\gamma}_{1,2}$, inside a circle with the effective Einstein radius around the center of the lens. Then, we subtract them from the original ones: $\delta\kappa_i \rightarrow \delta\kappa'_i = \delta\kappa_i - \delta\bar{\kappa}$ and $\delta\gamma_{i,1,2} \rightarrow \delta\gamma'_{i,1,2} = \delta\gamma_{i,1,2} - \delta\bar{\gamma}_{1,2}$.

Similarly, we also subtract the deflection angle arising from the mean external field. The convergence and the shear correspond to the second derivatives of the lensing potential while the deflection angle corresponds to the first derivative, and hence the constant shear corresponds to the deflection angle as a linear function of the angular coordinates (θ_1, θ_2) . First, we fit the deflection angle $\alpha(\theta_1, \theta_2)$ as a linear function of the angle (θ_1, θ_2) inside a circle with the Einstein radius. Since we assume the Born approximation, we evaluate the deflection angles along the unperturbed light rays. Then, we have $\alpha(\theta_1, \theta_2) \simeq \alpha_0 + \alpha_{11}\theta_1 + \alpha_{12}\theta_2$, where $\alpha_{0,11,12}$ are constants obtained from the fitting. Then, we subtract the

$\alpha_{0,11,12}$ terms from the original deflection angle: $\alpha(\theta_1, \theta_2) \rightarrow \alpha'(\theta_1, \theta_2) = \alpha(\theta_1, \theta_2) - \alpha_0 - \alpha_{11}\theta_1 - \alpha_{12}\theta_2$.

The angular positions of lensed images are shifted due to the lensing by the line-of-sight structures, but we expect that the shifts fall within observational errors if the image positions are well fit by the primary lens model. According to CASTLES database, the lensed image positions are typically measured within errors of ~ 0.003 arcsec. Then, the errors in the relative positions of any image pairs are $0.0042(= \sqrt{2} \times 0.003)$ arcsec. We only use samples in which the maximum shift of the relative angular positions among all the lensed images are less than $\varepsilon = 0.0042(= \sqrt{2} \times 0.003)$ arcsec in our analysis. If the shifts of positions due to perturbers in the line-of-sight are much larger than the observational error ε , we cannot reparametrise the model parameters to obtain a good fit. Even if one can fit one of the perturbed positions by reparametrisation, it is impossible to fit all the positions of lensed images provided that the surface density of the lens system has a nearly circular symmetry (see appendix A). Only allowed shifts are corresponding to the scale transformation that gives the mass-sheet degeneracy. However, we do not exclude the cases in which the order of shifts of images are $O(\varepsilon)$ as reparametrisation can improve the shifts by order $O(\varepsilon)$ in general.

Here, we adopt a circle with the effective Einstein radius around the lens as the background (or environment) of the lens. However, in real lens systems, the critical curves are elliptical and there is an ambiguity how to define the background. We will discuss these systematic uncertainties in Sec.7.6.

3) For all the images, we add the perturbed quantities as, $\kappa_i \rightarrow \kappa_i + \delta\kappa'_i$ and $\gamma_{i,1,2} \rightarrow \gamma_{i,1,2} + \delta\gamma'_{i,1,2}$, and then calculate the magnification contrast $\delta\mu_i/\mu_i$ from equation (7). We finally obtain the magnification perturbation η from equation (9).

4) In the previous procedures from 1) to 3), we choose an arbitrary grid point as the lens center. In order to obtain the probability distribution of η , we choose all the grid points (there are the 1000^2 points on a single map) as the lens centers. Note again that, to include the lens system in our analysis, we impose a condition that no massive line-of-sight halo in the neighborhood of the lens is allowed. We do not use the positions that are too close to the edges of the map (less than $10''$ from the edges) as the lens center, in order to calculate the maximum $\delta\kappa$ within a circle with a radius of $10''$ centred at the lens center (see the condition (i) in the procedure 1)). To increase the number of realisations, we also use maps rotated by 90, 180 and 270 degrees. Hence, we have 400 maps effectively.

5.3 Distribution of $\delta\bar{\kappa}$ and $\delta\bar{\gamma}$

As shown in Figure 5, the convergence perturbation $\delta\bar{\kappa}$ is negatively skewed if the shifts in the relative positions are constrained to satisfy $\delta\theta < 0.0042$ arcsec. This means that most of the constrained light-rays pass through underdense regions. The variances of PDFs of constrained convergence and shear perturbations are smaller than those of unconstrained ones, implying that effects of neighbouring massive structures are suppressed. For MG0414+0534

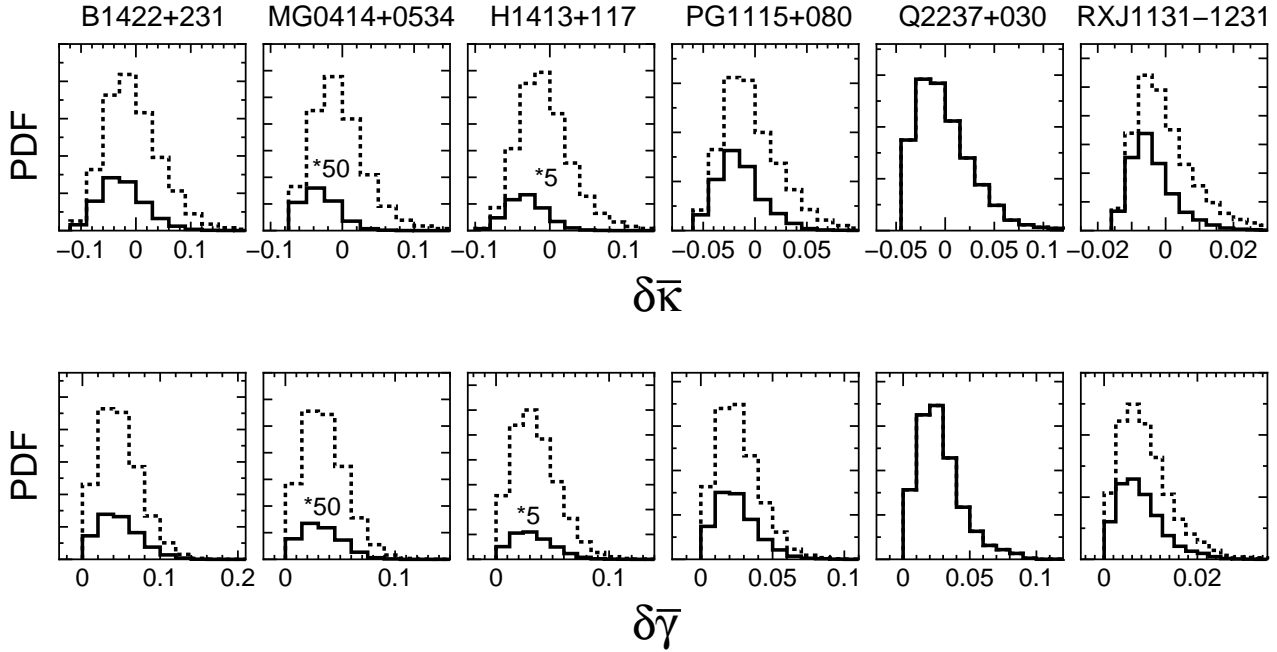


Figure 5. The PDFs of mean perturbed convergence $\delta\bar{\kappa}$ (red) and shear $\delta\bar{\gamma}$ (blue) for the six lens systems. The mean quantities ($\delta\bar{\kappa}$ and $\delta\bar{\gamma}$) are smoothed with a circular top-hat filter with the Einstein radius. The solid (dotted) lines are the PDFs with (without) the condition that shifts in the relative positions of pairs of lensed images are less than 0.0042 arcsec. Note that the convergence $\delta\bar{\kappa}$ can be positive or negative (corresponding to overdense or underdense regions), while the shear $\delta\bar{\gamma}$ is positive definite. For MG0414+0534 and H1413+117, the amplitudes of these quantities are multiplied by factors 50 and 5 (full curves).

and H1413+117, only a few light rays satisfy the constraint $\delta\theta < 0.0042$ arcsec. Since these two lens systems at high redshifts $z_L > 0.9$ have a large effective Einstein radius in comoving scale (see Tables 1 and 2), and large separation angles between lensed images, the projected density fluctuations induce larger shifts in lensed image positions (see also sec.6). As a result, only a few light rays satisfy the constraint. It can be interpreted that object Xs in these systems may reside in intergalactic spaces rather than in the primary lenses. In fact, Peng (2004) argues that much of the optical flux of object X in MG0414+0534 is actually coming from lensed images of the quasar host galaxy rather than object X itself. Our findings support this interpretation. For H1413+117, the perturber(s) may be a void(s) rather than a halo(s) in the intergalactic space since observed fluxes of images (B and C) with a positive parity are demagnified (Table 1).

6 ANALYTICAL FORMULATION

In this section, we present analytical formulation for estimating the weak-lensing effects by structures in the line-of-sight (see also IT12). The second moment of the magnification perturbation η can be calculated as follows.

The perturbed convergence $\delta\kappa$ and shear $\delta\gamma_{1,2}$ caused by density fluctuations along the line-of-sight are functions of a separation angle θ between a pair of lensed images. The

two-point correlation function of these perturbed quantities takes similar forms as those for evaluating the weak lensing effect by large-scale structures (e.g. Bartelmann & Schneider 2001). However, the unperturbed light-ray paths form a “diamond shape” connecting the observer and the source as shown in the orange lines in Fig. 2 because of strong lensing. Contribution from large-scale modes should be suppressed as it gives excess astrometric shifts between pairs of images. They should be constrained from errors in the relative positions of lensed images.

In a cosmological model with the Hubble constant H_0 and present matter density parameter $\Omega_{m,0}$, the constrained two-point correlation of $\delta\kappa$ as a function of a separation angle θ is

$$\begin{aligned} \xi_{\kappa\kappa}(\theta) &\equiv \langle \delta\kappa(0)\delta\kappa(\theta) \rangle \\ &= \frac{9H_0^4\Omega_{m,0}^2}{4c^4} \int_0^{r_S} dr r^2 \left(\frac{r-r_S}{r_S} \right)^2 [1+z(r)]^2 \\ &\quad \times \int_{k_{\text{lens}}}^{\infty} \frac{dk}{2\pi} k W^2(k) P_\delta(k, r) J_0(g(r)k\theta), \end{aligned} \quad (15)$$

where

$$g(r) = \begin{cases} r, & r < r_L \\ r_L(r_S - r)/(r_S - r_L), & r \geq r_L \end{cases} \quad (16)$$

and $P_\delta(k, r)$ is the power spectrum of dark matter density fluctuations as a function of the wavenumber k and the comoving distance r . r_S is the comoving distance to the source

and r_L to the lens from the observer and $z(r)$ is the redshift of a point at a comoving distance r . To calculate P_δ , we use the fitting function obtained from a high resolution cosmological simulation (Appendix of IT12, see also Smith et al. (2003); Takahashi et al. (2012)). The fitting function can be used up to a wavenumber $k = 300 h\text{Mpc}^{-1}$ within $\sim 20\%$ accuracy. J_0 is the zero-th order Bessel function and $g(r)\theta$ is the tangential separation between two unperturbed light-rays at a comoving distance r from the observer. Strictly speaking, this expression is not exact for sources that are shifted from the lens center. However, in what follows, we assume that the angular separation between the source and the lens center is sufficiently smaller than the effective Einstein radius of the primary lens so that the equation holds with good accuracy. The infrared cut-off scale in the wavenumber k_{lens} is given by the mean separation angle b between a lensed image and the lens center. For lens systems in which the primary lens dominates the lensing potential, it approximately equals to the effective Einstein radius b_E . We set the corresponding wavelength as $\lambda_{\text{lens}} = 4b$ or equivalently, $k_{\text{lens}} = \pi/2b$. Any modes whose fluctuation scales are larger than λ_{lens} contribute to the smooth component of the primary lens, namely, the constant convergence, shear and possible higher order ($m = 3, 4$) components. Therefore, we only consider fluctuation modes whose wavenumbers satisfy $k > k_{\text{lens}}$. Otherwise, double-counting of the constant convergence and shear leads to a systematically large perturbation.

The window function $W(k)$ has two cut-off scales in wavenumbers k_{cut} and k_{grid} . The cut-off scale k_{cut} is determined by the condition that the perturbation ε of angular separation between an arbitrary pair of lensed images should not exceed the observational error ε_{obs} for the maximum separation angle between lensed images. We consider the following two types of filtering. The first type is called the ‘‘sharp k-space (SK)’’ filter (see also IT12) in which the filter function satisfies

$$W_{\text{SK}}(k; k_{\text{cut}}) = \begin{cases} 0, & k < k_{\text{cut}} \\ 1, & k \geq k_{\text{cut}}. \end{cases} \quad (17)$$

Although the ‘‘sharp k-space’’ filtering is simple and easy for implementation, contributions from modes with $k_{\text{lens}} < k < k_{\text{cut}}$ may not be negligible. Therefore, we introduce another type of filtering so called the ‘‘constant shift (CS)’’ filter,

$$W_{\text{CS}}(k; k_{\text{cut}}) = \begin{cases} W_{\text{int}}(k), & k < k_{\text{cut}} \\ 1, & k \geq k_{\text{cut}}, \end{cases} \quad (18)$$

in which the corresponding contribution to the angular shifts between a pair of images with the maximum separation angle θ_{max} are constant in logarithmic interval in k for $k < k_{\text{cut}}$ (see Fig. 6). In this model, contribution from modes with $k_{\text{lens}} < k < k_{\text{cut}}$ to the angular shift ε does not depend on the wavenumber k (see also Appendix B for verification). W_{int} is explicitly given by

$$W_{\text{int}}^2(k; k_{\text{cut}}) \equiv \frac{\partial \varepsilon^2(W=1)}{\partial \ln k} \bigg/ \frac{\partial \varepsilon^2}{\partial \ln k} \bigg|_{k=k_{\text{cut}}}, \quad (19)$$

where

$$\varepsilon^2 = 2\langle \delta\theta^2(0) \rangle - 2\langle \delta\theta(0)\delta\theta(\theta_{\text{max}}) \rangle, \quad (20)$$

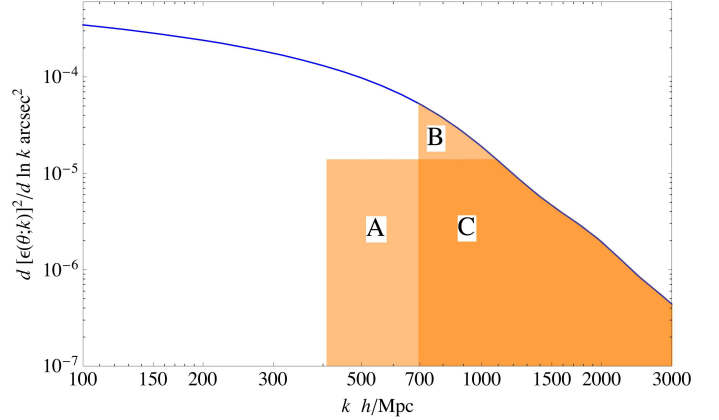


Figure 6. Window functions $W(k)$ for B1422+231. The upper boundary of the regions B and C corresponds to the values convolved with the sharp k-space (SK) filter with $k_{\text{cut}} = 694h/\text{Mpc}$ and those of the regions A and B, to the values convolved with the constant-shift (CS) cut with $k_{\text{cut}} = 1089h/\text{Mpc}$. Here we assume $k_{\text{lens}} = 408h/\text{Mpc}$.

and

$$\begin{aligned} \langle \delta\theta(0)\delta\theta(\theta) \rangle &= \frac{9H_0^4 \Omega_{m,0}^2}{c^4} \int_0^{r_S} dr \left(\frac{r - r_S}{r_S} \right)^2 [1 + z(r)]^2 \\ &\times \int_{k_{\text{lens}}}^{\infty} \frac{dk}{2\pi k} W^2(k) P_\delta(k; r) J_0(g(r)k\theta). \end{aligned} \quad (21)$$

The angular resolution of ray-tracing simulation is given by the grid size r_{grid} of the two dimensional gravitational potential. Fluctuations with angular sizes smaller than r_{grid} are strongly suppressed. For the TSC smoothing scheme, the input power spectrum is suppressed by a factor $\sim W_{\text{TSCiso}}^2(k; k_{\text{grid}}) = \exp(-\pi^2 k^2/k_{\text{grid}}^2)$, where $k_{\text{grid}} = 2\pi/r_{\text{grid}}$ (see Appendix for derivation). As shown in Fig. 7, the cut-off scale in comoving coordinates becomes small as the redshift of fluctuations decreases. This can be explained as follows. The comoving size of an arc that subtends a given angle become large as the distance to the arc increases. Therefore, if the angular size of the grids is fixed, the corresponding comoving size of grids becomes smaller as the distances to the grids decrease. Incorporating the finite grid-size effect for the TSC smoothing, the two types of filter function can be written as

$$W^2(k; k_{\text{cut}}, k_{\text{grid}}) = \begin{cases} W_{\text{SK}}^2(k; k_{\text{cut}}) W_{\text{TSCiso}}^2(k; k_{\text{grid}}) & \text{(SK)} \\ W_{\text{CS}}^2(k; k_{\text{cut}}) W_{\text{TSCiso}}^2(k; k_{\text{grid}}) & \text{(CS)}. \end{cases} \quad (22)$$

The two-point correlation functions for the other perturbed quantities are the same as in equation (15) except

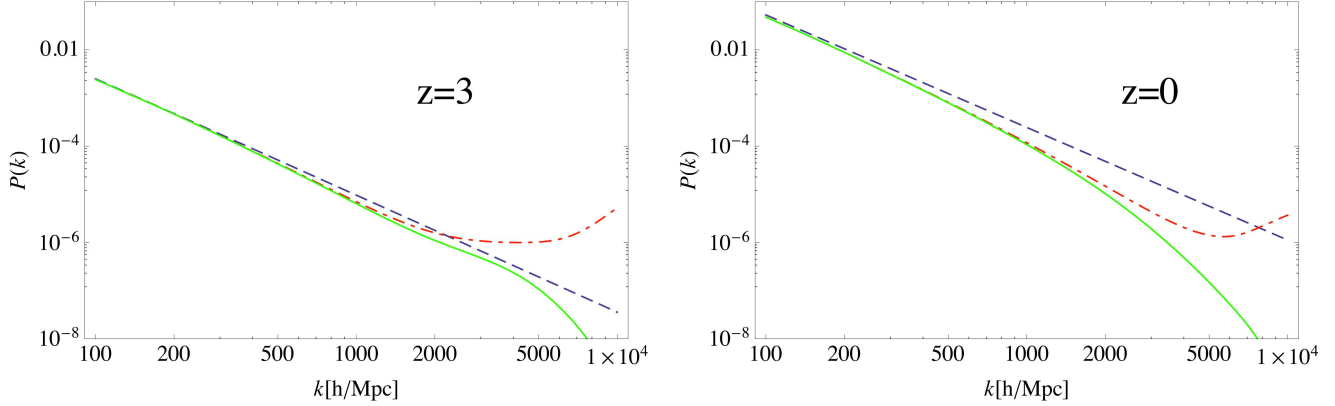


Figure 7. Power spectra $P(k)$ for $z = 3$ (left) and $z = 0$ (right). The plots of curves represent the fitting function in IT12 (blue dashed), an N -body simulation with $N_p^3 = 1024^3$ divided by the Cloud In Cell (CIC) window function, and the fitting function with the TSC smoothing with a grid size $r_{\text{grid}} = 0.6 h/\text{Mpc}$ (green full). An increase at small scales for the N -body simulation is due to the Poisson (shot) noise ($1/n = 9.3 \times 10^{-7} (N_p/1024)^{-3} h^{-3} \text{Mpc}^3$) and the division by the CIC window function.

for the J_0 term in the integrand:

$$\begin{aligned}
 \langle \delta\gamma_1(0)\delta\gamma_1(\boldsymbol{\theta}) \rangle &: J_0 \rightarrow \frac{1}{2} [J_0 + J_4 \cos(4\phi_\theta)], \\
 \langle \delta\gamma_2(0)\delta\gamma_2(\boldsymbol{\theta}) \rangle &: J_0 \rightarrow \frac{1}{2} [J_0 - J_4 \cos(4\phi_\theta)], \\
 \langle \delta\kappa(0)\delta\gamma_1(\boldsymbol{\theta}) \rangle &: J_0 \rightarrow -J_2 \cos(2\phi_\theta), \\
 \langle \delta\kappa(0)\delta\gamma_2(\boldsymbol{\theta}) \rangle &: J_0 \rightarrow -J_2 \sin(2\phi_\theta), \\
 \langle \delta\gamma_1(0)\delta\gamma_2(\boldsymbol{\theta}) \rangle &: J_0 \rightarrow \frac{1}{2} J_4 \sin(4\phi_\theta),
 \end{aligned} \tag{23}$$

where the Bessel functions $J_{0,2,4}$ are functions of $g(r)k\theta$ and $\boldsymbol{\theta} = (\theta \cos \phi_\theta, \theta \sin \phi_\theta)$. When the separation angle θ between a pair of lensed images is sufficiently smaller than θ_E , the terms which are proportional to J_2 or J_4 are sufficiently smaller than J_0 . In this case, we can drop these terms and hence from equations (15) and (23), we have $\langle \delta\gamma_1\delta\gamma_1 \rangle = \langle \delta\gamma_2\delta\gamma_2 \rangle = \xi_{\kappa\kappa}/2$ and $\langle \delta\kappa\delta\gamma_1 \rangle = \langle \delta\kappa\delta\gamma_2 \rangle = \langle \delta\gamma_1\delta\gamma_2 \rangle = 0$.

From equations (8) and (9), we can obtain the second moment of η . As an example, let us consider three images with two minima A and C and one saddle B with $\kappa_B < 1$. Choosing coordinates where the separation angle is perpendicular to + mode (i.e., $\theta \sin \phi_\theta = 0$), we have $\langle \delta\kappa\delta\gamma_2 \rangle = \langle \delta\gamma_1\delta\gamma_2 \rangle = 0$. Then, for $|\delta_i^\mu| \ll 1$, the second moment $\langle \eta^2 \rangle$ can be written as

$$\begin{aligned}
 \langle \eta^2 \rangle &= \frac{1}{4} \left[(I_A + I_B) - 2I_{AB}(\theta_{AB}) + (I_B + I_C) \right. \\
 &\quad \left. - 2J_{BC}(\theta_{BC}) \right],
 \end{aligned} \tag{24}$$

where

$$I_i \equiv \mu_i^2 (4(1 - \kappa_i)^2 + 2\gamma_{1i}^2 + 2\gamma_{2i}^2) \xi_\kappa(0), \tag{25}$$

and

$$\begin{aligned}
 I_{ij}(\theta) &\equiv 4\mu_i\mu_j \left[(1 - \kappa_i)(1 - \kappa_j) \xi_\kappa(\theta) \right. \\
 &\quad + \gamma_{1i}\gamma_{1j} \langle \delta\gamma_1(0)\delta\gamma_1(\boldsymbol{\theta}) \rangle + \gamma_{2i}\gamma_{2j} \langle \delta\gamma_2(0)\delta\gamma_2(\boldsymbol{\theta}) \rangle \\
 &\quad + (1 - \kappa_i)\gamma_{1j} \langle \delta\kappa_i(0)\delta\gamma_{1j}(\boldsymbol{\theta}) \rangle \\
 &\quad \left. + (1 - \kappa_j)\gamma_{1i} \langle \delta\kappa_j(0)\delta\gamma_{1i}(\boldsymbol{\theta}) \rangle \right],
 \end{aligned} \tag{26}$$

for $i = A, B, C$. In a similar manner, for a four-image system with two minima A and C and two saddles B and D with $\kappa_B < 1$ and $\kappa_D < 1$, the second moment is given by

$$\begin{aligned}
 \langle \eta^2 \rangle &= \frac{1}{8} \left[I_A + I_B - 2I_{AB}(\theta_{AB}) + (I_C + I_D) \right. \\
 &\quad - 2I_{CB}(\theta_{CB}) + (I_A + I_D) - 2I_{AD}(\theta_{AD}) \\
 &\quad \left. + (I_C + I_D) - 2I_{CD}(\theta_{CD}) \right],
 \end{aligned} \tag{27}$$

where I_i and $I_{ij}(\theta)$, $i = A, B, C, D$ are given by (25) and (26). Note that we are using coordinates in which $\phi_\theta = 0$.

7 RESULTS

7.1 Probability distribution of η

In this section, we present the results of our simulation. First we show the probability distribution function (PDF) of η , the mean $\langle \eta \rangle$ and the second moment $\langle \eta^2 \rangle$, and then we discuss the numerical convergence of our simulation. Note that the magnification perturbation η is defined in equation (9). Fig. 8 shows the PDFs of η for the six lens systems. Each colored histogram shows the PDFs with different grid sizes of $r_{\text{grid}} = 4.8h^{-1}\text{kpc}$ (green), $2.4h^{-1}\text{kpc}$ (blue), $1.2h^{-1}\text{kpc}$

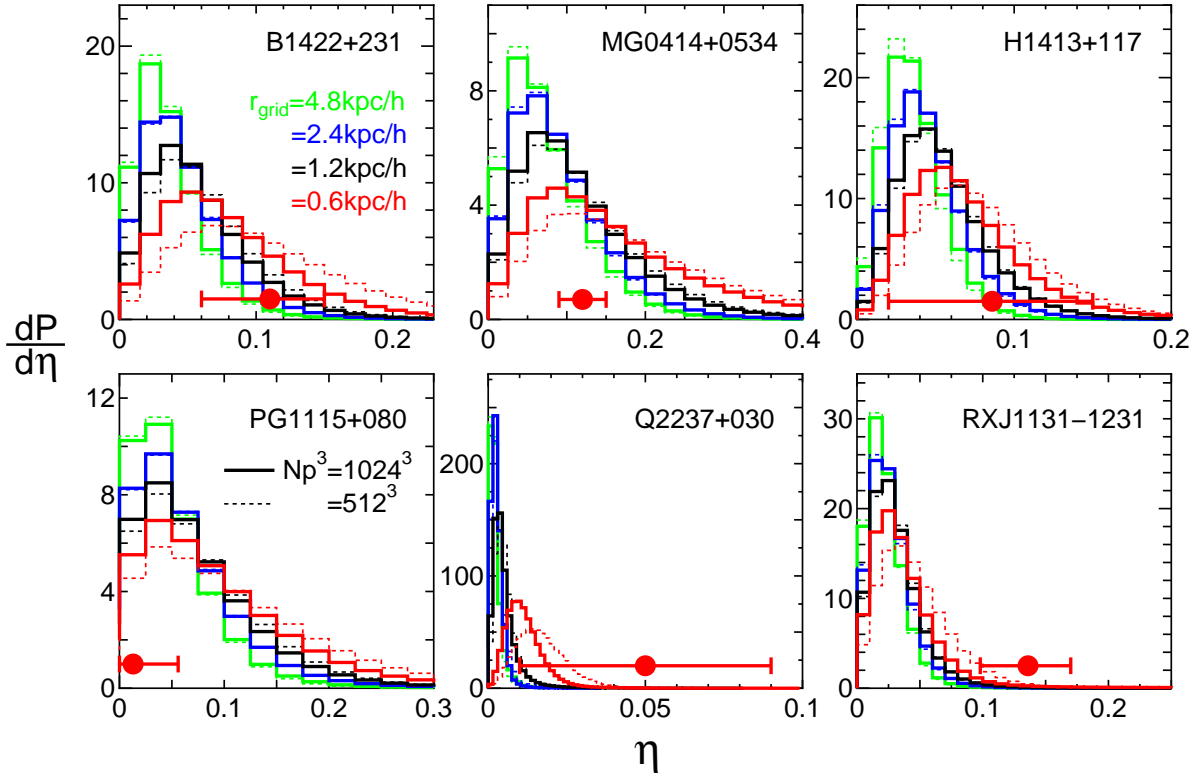


Figure 8. The PDF of η for the six lens systems. The histograms are our simulation results of the 1024^3 particles (solid lines) and 512^3 particles (dotted lines) with the grid resolution $r_{\text{grid}} = 4.8$ (green), 2.4 (blue), 1.2 (black) and $0.6h^{-1}\text{kpc}$ (red), respectively. The red filled circles with error bars denote the observational data with the 1σ error.

(black), and $0.6h^{-1}\text{kpc}$ (red). The solid and dotted lines correspond to the different numbers of N -body particles, $N_p^3 = 1024^3$ (solid) and 512^3 (dotted). Each PDF is normalised to unity. The red filled-circles with horizontal error bars (1σ) correspond to the observational data. Note that uncertainty of the primary lens is not taken into account for determining the errors of η . On smaller grid scales, the PDFs become larger and have a longer tail at large η . As clearly seen in Fig. 8, our simulation results are consistent with the observed data.

We check the numerical convergence of our simulation by comparing the high (low) resolutions of $N_p^3 = 1024^3$ (512^3) particles. The solid (dotted) lines in Fig. 8 are the results for $N_p^3 = 1024^3$ (512^3). As clearly seen in Fig. 8, the results with $N_p^3 = 1024^3$ agree with those with 512^3 in which $r_{\text{grid}} = 4.8, 2.4$ and $1.2h^{-1}\text{kpc}$ for all the systems. However, in the smallest grid size $r_{\text{grid}} = 0.6h^{-1}\text{kpc}$, with $N_p^3 = 512^3$, the distribution is clearly broader than that with $N_p^3 = 1024^3$ for the all systems. This is because, for small number of particles, the shot noise dominates the power spectrum and hence the PDF becomes wider. The contribution of shot noise to the second moment $\langle \eta^2 \rangle$ can be analytically estimated by replacing the power spectrum $P_\delta(k, r)$ in equation (15) with $P_\delta(k, r) + 1/n$ where n is the number density of N -body particles and $1/n$ corresponds to the shot noise. For the grid size $r_{\text{grid}} = 0.6h^{-1}\text{kpc}$ with $N_p^3 = 512^3$,

the shot noise dominates the signal. For the larger grid sizes $r_{\text{grid}} \geq 1.2h^{-1}\text{kpc}$, the small-scale P_δ and the shot noise do not contribute to the integral of $\langle \eta^2 \rangle$ in equation (15) due to the window function, and hence we can neglect the shot noise even for $N_p^3 = 512^3$. In what follows, we use the result of our simulation with parameters $N_p = 1024^3$ and $r_{\text{grid}} = 1.2h^{-1}\text{kpc}$ as a fiducial model.

Table 3 shows the mean and the rms of η obtained from the high resolution simulation ($N_p^3 = 1024^3$) and the analytical calculation using two types of window function, “sharp-k space”(SK) and “constant shift”(CS) cut. In the 1st column, we plot the observed η and the mean with au the 1σ error, in the 2nd column, the grid sizes from $r_{\text{grid}} = 0.6h^{-1}\text{kpc}$ (top) to $4.8h^{-1}\text{kpc}$ (bottom), in the 3rd and 4th columns, the mean η with the 1σ error and the rms of η obtained from the simulation (in calculating these statistical quantities from the simulation, we use the data up to $\eta = 0.5$ to cut the long tail in the PDF⁵), in the 5th column, the rms of η from the analytical calculation discussed in sec.6. Our simu-

⁵ We find that 99.4% of our samples satisfy $\eta \leq 0.5$ for all the six lens systems in our fiducial simulation model ($N_p^3 = 1024^3$ with grid size $r_{\text{grid}} = 1.2h^{-1}\text{pc}$). If we further add samples that satisfy $0.5 < \eta \leq 1$, $\langle \eta^2 \rangle^{1/2}$ increase by 11% for MG0414, by 2.5% for PG1115 and by $< 0.21\%$ for the others. This is because the PDFs of MG0414 and PG1115 have a relatively longer tail as shown in

Table 3. Mean and rms of η for various grid sizes r_{grid}

lens system	$r_{\text{grid}}(h^{-1}\text{kpc})$	$\langle\eta\rangle \pm \Delta\eta(\text{sim.})$	$\langle\eta^2\rangle^{1/2}(\text{sim.})$	$\langle\eta^2\rangle^{1/2}(\text{CS})$	$\langle\eta^2\rangle^{1/2}(\text{SK})$
B1422+231 $\eta_{\text{obs}} = 0.11^{+0.04}_{-0.05}$	0.6	0.081 ± 0.053	0.097	0.138	0.141
	1.2	0.058 ± 0.038	0.069	0.117	0.120
	2.4	0.047 ± 0.031	0.056		
	4.8	0.037 ± 0.026	0.044		
MG0414+0534 $\eta_{\text{obs}} = 0.12 \pm 0.03$	0.6	0.158 ± 0.103	0.188	0.160	0.182
	1.2	0.114 ± 0.076	0.137	0.129	0.151
	2.4	0.091 ± 0.060	0.109		
	4.8	0.075 ± 0.053	0.092		
H1413+117 $\eta_{\text{obs}} = 0.086^{+0.064}_{-0.066}$	0.6	0.072 ± 0.044	0.084	0.065	0.073
	1.2	0.055 ± 0.029	0.062	0.052	0.061
	2.4	0.046 ± 0.025	0.052		
	4.8	0.037 ± 0.019	0.041		
PG1115+080 $\eta_{\text{obs}} = 0.013^{+0.043}_{-0.013}$	0.6	0.090 ± 0.076	0.118	0.132	0.135
	1.2	0.070 ± 0.060	0.093	0.115	0.121
	2.4	0.059 ± 0.051	0.078		
	4.8	0.047 ± 0.042	0.063		
Q2237+030 $\eta_{\text{obs}} = 0.05 \pm 0.04$	0.6	0.0120 ± 0.0111	0.0163	0.011	0.011
	1.2	0.0053 ± 0.0049	0.0072	0.002	0.002
	2.4	0.0027 ± 0.0021	0.0034		
	4.8	0.0021 ± 0.0021	0.0030		
RXJ1131-1231 $\eta_{\text{obs}} = 0.136^{+0.034}_{-0.038}$	0.6	0.040 ± 0.041	0.058	0.071	0.072
	1.2	0.031 ± 0.021	0.037	0.064	0.065
	2.4	0.027 ± 0.017	0.032		
	4.8	0.022 ± 0.015	0.027		

lation results of $\langle\eta^2\rangle^{1/2}$ agree with the analytical ones within $\lesssim 40$ percent. The SK cut gives systematically smaller values than the CS cut. The difference between SK and CS is conspicuous only for MG0414+0534 and H1413+117 where the comoving size of the lens is large. Otherwise, the difference is negligible. For the larger source redshift, the magnification perturbation η is larger. For Q2237+030, both the lens redshift and the effective Einstein radius (in the comoving scale) are the smallest, the magnification perturbation is found to be very small.

7.2 Fitting Formula for PDF of η

As mentioned in introduction, density fluctuations of dark matter on very small scales ($< 10h^{-1}\text{kpc}$) are strongly non-Gaussian. As a result, the perturbed convergence $\delta\kappa$, shear $\delta\gamma$ and the magnification perturbation η obey non-Gaussian statistics. Although the analytical formula for the second moment of η was derived in IT12, it is not sufficient to describe non-Gaussian nature of η . In order to do so, we derive a fitting formula for the PDF of η using our simulated data. The PDF is also used to obtain higher order moments of η such as the skewness and kurtosis. These statistics contain important information about the dark matter clustering on very small scales.

Based on ray-tracing simulations, some authors suggested that the PDFs of convergence and shear in-

duced by the large scale structures are well approximated by the log-normal distribution (e.g., Jain et al. 2000; Taruya et al. 2002; Das & Ostriker 2006; Hilbert et al. 2007; Takahashi et al. 2011). This fact reflects that the one-

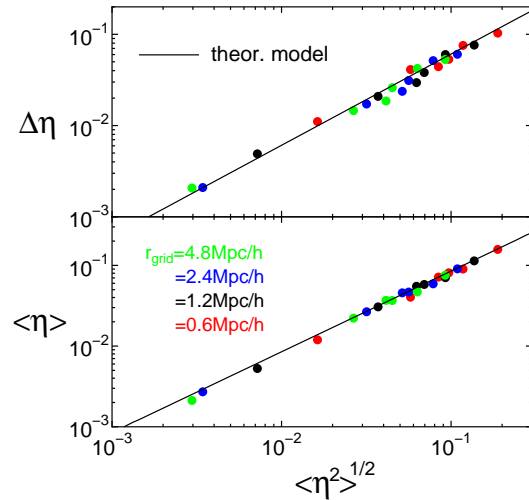


Figure 10. The variance $\Delta\eta$ and the mean $\langle\eta\rangle$ as a function of the rms $\langle\eta^2\rangle^{1/2}$. The colored symbols are the simulation results for the six lens systems with various grid sizes. The solid lines are the theoretical prediction of the log-normal PDF.

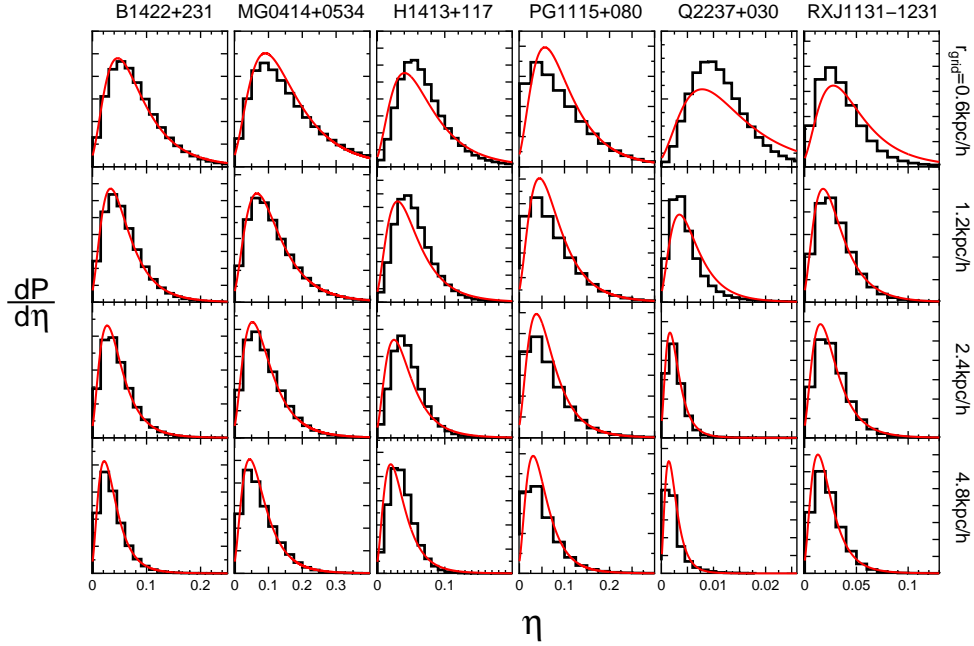


Figure 9. The fitting formula for the PDF of η for the six lens systems. The red curves are the log-normal fitting function, while the black histograms are the simulation results for 1024^3 particles with various grid sizes $r_{\text{grid}} = 0.6 - 4.8 h^{-1} \text{kpc}$.

point distribution function of the matter density field is also well described by the log-normal distribution (e.g., Coles & Jones 1991; Kofman et al. 1994; Kayo et al. 2001). As η is proportional to $\delta\kappa$ and $\delta\gamma$ for $\eta \ll 1$, we use the log-normal function for fitting the PDFs of η ,

$$\frac{dP}{d\eta} = N \exp \left[-\frac{1}{2\sigma^2} \left\{ \ln \left(1 + \frac{\eta}{\eta_0} \right) - \ln \mu \right\}^2 \right] \frac{1}{\eta + \eta_0}, \quad (28)$$

where N is a normalisation constant, η_0 describes a dispersion scale of η , and σ and μ are kept to be constant⁶. We assume that the fitting formula depends only on the second moment $\langle \eta^2 \rangle$. In fact, the PDF may depend on various factors such as the source and lens redshifts, the image positions, and the lens parameters. However, the most important parameter that characterises the PDF is the second moment $\langle \eta^2 \rangle$, and hence we simply ignore the other factors. Then we can calculate $\langle \eta^2 \rangle$ using equation (28) as,

$$\langle \eta^2 \rangle = \int_0^\infty d\eta \frac{dP}{d\eta} \eta^2 \propto \eta_0^2, \quad (30)$$

⁶ Taruya et al. (2001) showed that the PDF of the convergence $\delta\kappa$ is well fitted by the following log-normal function,

$$\frac{dP}{d\delta\kappa} = N_\kappa \exp \left[-\frac{1}{2\sigma_\kappa^2} \left\{ \ln \left(1 + \frac{\delta\kappa}{|\delta\kappa_{\text{min}}|} \right) + \frac{\sigma_\kappa^2}{2} \right\}^2 \right] \frac{1}{\delta\kappa + |\delta\kappa_{\text{min}}|}, \quad (29)$$

where $\delta\kappa_{\text{min}}$ is the minimum convergence for the empty beam (e.g., Jain et al. 2000) and σ_κ is the variance of $\delta\kappa$. Our fitting formula in equation (28) is based on equation (29), but simply replace the variable $\delta\kappa$ to η and add a term $\ln \mu$ instead of $\sigma_\kappa^2/2$ in the exponential to give a better fit at $\eta \sim 0$.

and hence $\eta_0 \propto \langle \eta^2 \rangle^{1/2}$. Then we fit three parameters σ , μ and $\eta_0/\langle \eta^2 \rangle^{1/2}$ to minimize the chi-square

$$\chi^2 = \sum_{\text{lens}} \sum_{r_{\text{grid}}} \sum_{\eta} \frac{(dP_{\text{model}}/d\eta - dP_{\text{sim}}/d\eta)^2}{(dP_{\text{model}}/d\eta)^2} \delta\eta \quad (31)$$

where $dP_{\text{model}}/d\eta$ and $dP_{\text{sim}}/d\eta$ are the PDFs for the log-normal model and the simulation results, respectively, and $\delta\eta$ is the bin-width in the simulation results of the PDFs. The summation is performed over all the six lens systems, the four grid sizes $r_{\text{grid}} = 0.6 - 4.8 h^{-1} \text{kpc}$, and η . Then, we find the best-fit parameters as,

$$\mu = 4.10, \quad \sigma^2 = 0.279, \quad \eta_0 = 0.228 \langle \eta^2 \rangle^{1/2}, \quad (32)$$

where the second moment $\langle \eta^2 \rangle$ is obtained from the simulation (see Table 3). Fig. 9 shows our best-fit model (red curves) and the simulation results (black histograms). The best-fit model is in agreement with the simulation results within an error of $\lesssim 30\%$.

Using the log-normal PDF in equation (28), one can easily verify that the n -th moment of η , $\langle \eta^n \rangle$, is proportional to η_0^n . Then, equation (30) implies that the mean $\langle \eta \rangle$ and the standard deviation $\Delta\eta$ are also proportional to η_0 and the rms of η , $\langle \eta^2 \rangle^{1/2}$. The relations between these variables can be seen in Fig. 10. The horizontal axis denotes $\langle \eta^2 \rangle^{1/2}$ and the vertical axis shows the standard deviation $\Delta\eta$ and the mean $\langle \eta \rangle$, respectively. The colored dots are the simulation results for the six lens systems with various grid sizes. The solid straight lines correspond to the theoretical values based on the log-normal PDF. Equation (28) and the best-fit parameters in equation (32) lead to

$$\Delta\eta = 0.608 \langle \eta^2 \rangle^{1/2}, \quad \langle \eta \rangle = 0.850 \langle \eta^2 \rangle^{1/2}. \quad (33)$$

Table 4. Standard deviation and skewness of $\delta\mu/\mu$

lens system	image	parity	deviation σ	skewness S
B1422+231	A	+	0.074	0.86
	B	-	0.072	0.31
	C	+	0.052	0.82
MG0414+0534	A1	+	0.14	0.73
	A2	-	0.15	0.34
	B	+	0.067	1.3
H1413+117	A	-	0.078	0.18
	B	+	0.062	0.91
	C	+	0.064	1.1
	D	-	0.032	0.042
PG1115+080	A1	+	0.089	0.83
	A2	-	0.056	0.25
Q2237+030	A	+	0.0067	0.62
	B	+	0.010	0.54
	C	-	0.0030	0.10
	D	-	0.0065	0.20
RXJ1131-1231	A	-	0.045	-0.0071
	B	+	0.033	1.3
	C	+	0.035	1.1

As shown in Fig. 10, these best-fit parameters give good approximations of $\Delta\eta$ and $\langle\eta\rangle$ as a function of $\langle\eta^2\rangle^{1/2}$, which can be estimated using the analytical formulae in section 6. As these values do not depend on complex parameters of each lens system, it may be considered as the “universal” relation which is applicable to all quadruple lens systems.

7.3 PDF of magnification contrast

This section shows the simulation results for the PDFs of magnification contrast $\delta\mu/\mu$ for each image in the six lens systems (Fig. 11). We find that the changes in the fluxes are typically $\sim 1 - 10\%$, and the magnification contrast $\delta\mu/\mu$ is larger for systems with a higher source redshift. For Q2237, the nearest lens at $z_L = 0.04$ is exceptionally small in comparison with the other lens systems, the flux change is quite small because the relevant comoving size of the lens is significantly small in comparison with the other lens systems. The PDF of $\delta\mu/\mu$ is broader for brighter images, because the magnification perturbation is proportional to the unperturbed magnification due to the primary lens, $\delta\mu_i/\mu_i \propto \mu_i$, which can be shown by using equations (7) and (8). The standard deviations of $\delta\mu/\mu$, $\sigma^2 = \langle(\delta\mu/\mu - \langle\delta\mu/\mu\rangle)^2\rangle$, are listed in the 3rd column in Table 4. The means of $\delta\mu/\mu$ are consistent to be zero. Table 4 also show the skewness, $S = \langle(\delta\mu/\mu - \langle\delta\mu/\mu\rangle)^3\rangle/\sigma^{3/2}$, in the 4th column. If the PDF of $\delta\mu/\mu$ obeys Gaussian statistics, the skewness vanishes. In calculating the above moments, we use the range $|\delta\mu/\mu| < 0.5$. As shown in Table 4, the skewness for images with a positive parity is systematically larger than those with a negative parity. This reflects the fact that images with a positive parity tend to be magnified by a halo while those with a negative parity are either magnified or demagnified by a halo at the linear regime depending on the positions of the perturbers. Although the number of halos are smaller than that of voids, the amplitude of the density contrast due

to halos can be higher than that due to voids. Therefore, we have a positive skewness for images with a positive parity. On the other hand, for images with a negative parity, halos can demagnify the image. Hence, the skewness becomes small in comparison with the images with a positive parity. If the perturber is a void, then images with a positive parity are demagnified and those with a negative parity are either magnified or demagnified. If the origin of the flux anomaly is the weak lensing effect due to the line-of-sight structures rather than subhalos, we would observe these patterns in flux changes if perturbed by voids. However, the number of our sample is not enough to confirm such cases.

7.4 Mass scales of intervening structures

In this subsection, we estimate the mass scales of intervening structures in 6 quasar-galaxy lens systems. In Fig.12, we plot the PDFs of surface mass δM due to intervening structures per arcsec² for all the lens systems. The horizontal axis is the intervening surface mass (in unit of $10^8 M_\odot$) per arcsec². The surface mass density is obtained from the convergence perturbation $\delta\kappa'$ using the relation (e.g. Schneider et al. 1992), $\delta M = \delta\kappa' \Sigma_{\text{cr}} D_j^2$, where Σ_{cr} is the critical mass density and D_j is the angular diameter distance to the intervening structure on the j-th lens plane (see Fig.1). Then we have,

$$\delta M = 1.17 \times 10^9 h^{-1} M_\odot \text{arcsec}^{-2} \left(\frac{\delta\kappa'}{0.01} \right) \frac{H_0 D_j D_S}{D_{jS}}, \quad (34)$$

where D_{jS} and D_S are the angular diameter distances from the j-th lens plane and the observer to the source, respectively. The upper horizontal axes of Fig.12 show the corresponding convergence perturbations $\delta\kappa'$. For obtaining the convergence perturbations $\delta\kappa'$, we subtract the mean convergence within the effective Einstein radius of the primary lens (see sec. 5.2). In order to estimate the surface mass density, we assume that $D_j = D_{jS}$ in equation (34) where the contribution becomes maximal. The results simply scale as $\delta M \propto D_j/D_{jS}$ if $D_j \neq D_{jS}$. Therefore, the obtained values should be interpreted as the upper limits.

As shown in Fig.12, the obtained surface mass densities are $O[10^{7-8}] M_\odot \text{arcsec}^{-2}$ and the contribution from negative masses (voids) are comparable to that from positive masses (halos). As the distance to the source increases (decreases), or the comoving size of the lens increases (decreases), the projected mass of intervening structures gets larger (smaller). The result clearly shows that the lens systems with a high redshift source or a massive lens are much affected by the line-of-sight structures.

Although the convergence perturbations are independent on angular positions due to the spatial homogeneity of perturbations, there are tiny differences between the PDFs within one single lens system. This is because that 1) we subtract the mean convergence perturbation around the lens center and hence $\delta\kappa'$ depends on the angular positions with respect to the lens center, and 2) we also impose various conditions (see sec.5.2).

In our model, the effect of structures whose sizes are equal to or larger than the size of the primary lens is taken into account as part of the primary lens (e.g. external shear, constant convergence). Therefore, the angular sizes of the “background” intervening structures are smaller than the

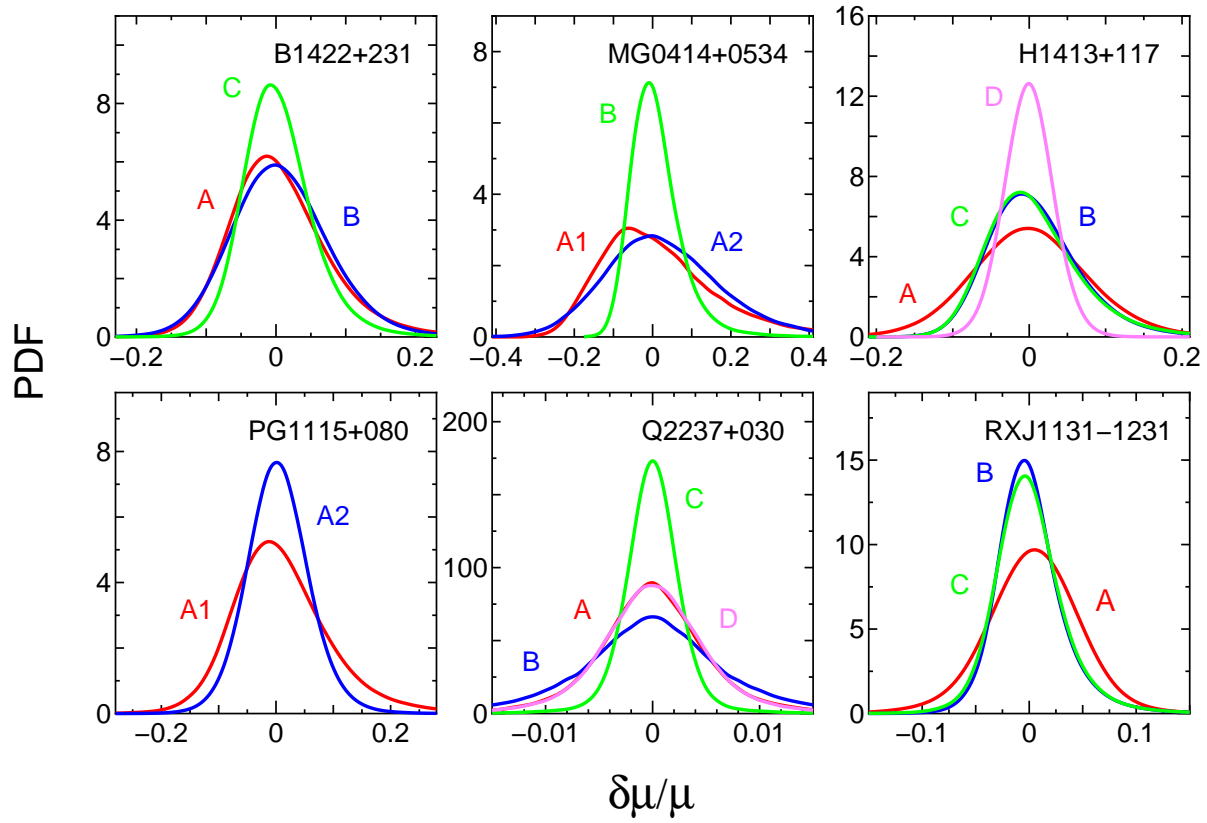


Figure 11. The PDF of the magnification contrast $\delta\mu/\mu$ of each image. Each colored curve corresponds to the PDF of each image A,B,C... The simulation results are for 1024^3 particles with the grid size $r_{\text{grid}} = 1.2h^{-1}\text{kpc}$.

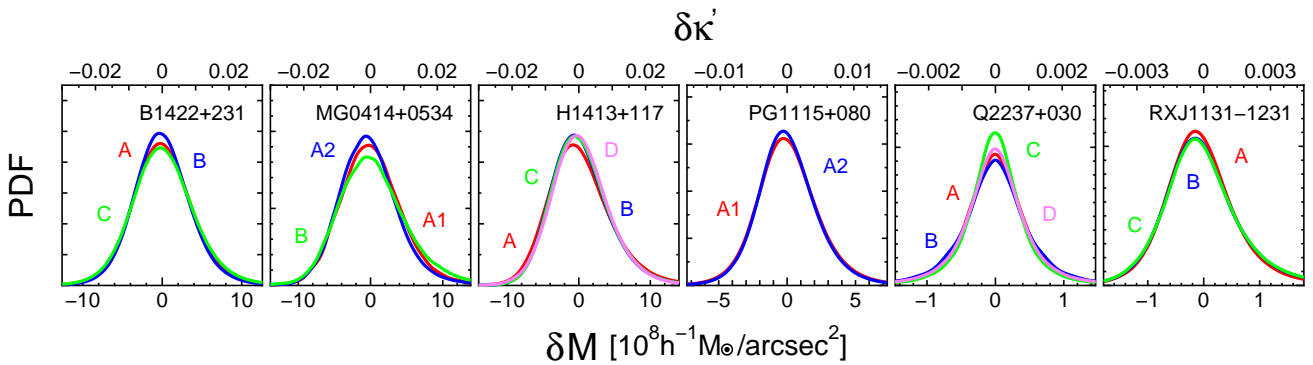


Figure 12. The PDFs of the approximated surface mass density of intervening structures δM per arcsec², in unit of $10^8 M_{\odot}$. We assume that $D_j = D_{jS}$ in equation (34) where the contribution becomes maximal. Each colored curve corresponds to δM along the line-of-sight to each image. The upper horizontal axes also show the corresponding convergence perturbation. The simulation results are for 1024^3 particles with a grid size $r_{\text{grid}} = 1.2h^{-1}\text{kpc}$.

size of the primary lens, and hence their mass scales (void or halo) are $\lesssim 10^8 M_\odot$.

7.5 Comparison with Observed Flux Ratios

In this subsection, we compare our theoretically predicted flux ratios for 1024^3 particles with $r_{\text{grid}} = 1.2h^{-1}$ kpc to the observed values for the 6 MIR lens systems (Fig. 13). The horizontal and vertical axes are the flux ratios except for PG1115+080 where the PDF as a function of the flux ratio $A1/A2$ is plotted, the black crosses show the best-fit values that describe the primary lens models, the black contours around the crosses correspond to 1σ , 2σ , and 3σ confidence regions due to intervening structures, and the red filled-circles with bars are the measured results with the 1σ observational error. The predicted flux ratios are in good agreement with the observed values at $1 \sim 2\sigma$ level. Thus, the intervening structures can provide sufficient magnification perturbations in order to explain the anomalies in the flux-ratios.

7.6 Systematics

Finally, we comment on some systematics in our simulations. In our procedure, we impose various conditions and assumptions on our simulations in evaluating the magnification perturbations. In this section, we investigate the effects of these conditions on our results. We present the results only for B1422+231 with $r_{\text{grid}} = 1.2h^{-1}$ kpc, but we expect that similar results hold for the other lens systems.

In our simulations, we impose a condition that massive line-of-sight halos do not reside around a lens (see section 5.2) since the magnification perturbation would be too large if they are included. Furthermore, we impose the following two conditions: (i) maximum perturbed convergence within a circle with an angular radius $10''$ centered at the lens center is less than 0.5, and (ii) perturbed convergence and shear within a circle with the effective Einstein radius of the primary lens centered at the lens center should be less than those of the primary lens (see procedure 1) in section 5.2). If we do not impose these conditions, the mean and rms of η systematically change $\sim 1\%$ at most. Similarly, we also impose that the relative shifts in positions of lensed images due to the line-of-sight structures should be less than $0.0042''$. Without this condition, the rms of η increases by about 60% ($\langle \eta^2 \rangle^{1/2} = 0.069$ increases to 0.11). Hence, the constraint on angular shifts of lensed images significantly influences the magnification perturbations.

In section 5.2, procedure 2), we added the perturbed convergence $\delta\kappa$ and shear $\delta\gamma_{1,2}$ to κ and $\gamma_{1,2}$ in the primary lens. Then, we subtracted the mean perturbed convergence $\delta\bar{\kappa}$ and shear $\delta\bar{\gamma}_{1,2}$ around the lens from $\delta\kappa$ and $\delta\gamma_{1,2}$. This is because that the primary lens model already includes the external shear and constant density. Similarly, we also subtract the mean perturbed deflection-angles for the same reason. To calculate the mean of perturbed quantities, we average them over a region within a circle with an effective Einstein radius θ_E of the primary lens centered at the primary lens center. However, it is not simple to divide a complex lens system into the ‘‘external’’ and ‘‘internal’’ parts. For instance, actual lenses generally have a non-zero ellipticity, and the

light-ray paths around a lens center are not so simple as discussed in section 3.2. To check how these uncertainties would affect our result, we calculate mean quantities over regions with circle radii, $2\theta_E$ and $3\theta_E$. Then the rms’s of magnification perturbation η are found to be $\langle \eta^2 \rangle^{1/2} = 0.069, 0.077$ and 0.092 for $\theta_E, 2\theta_E$ and $3\theta_E$, respectively. Hence, such ambiguity would change the magnification perturbations by ~ 20 percent.

It is also important to comment on the mass-sheet degeneracy in the lens model. The flux ratios for the primary lens (without perturbations) are invariant under the transformation, $1 - \kappa_i \rightarrow \lambda(1 - \kappa_i)$, $\gamma_{i1,2} \rightarrow \lambda\gamma_{i1,2}$ and $\beta \rightarrow \lambda\beta$ where λ is a constant (Falco et al. 1985). Under this transformation, the magnification perturbation is transformed as $\eta \rightarrow \lambda^{-1}\eta$ and $\delta\mu_i/\mu_i \rightarrow \lambda^{-1}\delta\mu_i/\mu_i$. As the typical amplitude of the background shear on a scale of an Einstein radius $\theta_E = 1''$ (the typical size of a lens in our samples) is $\gamma \lesssim 0.1$ (see Fig. 5), the degeneracy affects η by $\lesssim 10$ percent.

In our ray-tracing simulation, we assumed the Born approximation which has some limitations and systematics. Under the approximation, we cannot investigate the strong lensing effects by the intervening objects such as image-position shifts and strong image deformations. Especially, the image-position shifts are very important, since we can separate the contributions from the main lens and the intervening lenses by fitting the image positions and then we can correctly estimate the magnification perturbations induced by the intervening objects. As a result, our conclusions would strongly depend on this approximation and hence we are planning to re-calculate the simulations without the Born approximation.

8 CONCLUSION AND DISCUSSION

We have investigated the weak lensing effects of line-of-sight structures in quadruple lens systems. We have run ray-tracing simulations to evaluate the magnification perturbations of quadruply lensed images. The magnification ratios typically change by $O(10\%)$ when the shifts of relative angular positions of quadruple lensed images are constrained to $< 0.004''$. We have found that the probability of having such small shifts is extremely small for MG0414+0534 and H1413+117. Therefore, it is likely that object X in these systems are residing in the intergalactic space rather than the neighbourhood of lensing galaxies. The constrained amplitudes of projected density perturbations due to line-of-sight structures are $O(10^8) M_\odot/\text{arcsec}^2$. These results are consistent with our new analytical estimate that intervening structures can perturb the magnifications of lensed images to explain the observed anomalies in the flux ratios of quadruple lenses. We have found that the constrained mean amplitudes of projected density perturbations in the line-of-sight are negative, which suggests that the lensed images are perturbed by minivoids and minihalos in underdense regions and approximately 50 percent of systems are perturbed by voids rather than haloes. Thus the role of voids or underdense regions in the line-of-sight is important in order to understand the origin of anomaly in the flux ratios. We have derived a new fitting formula for evaluating the PDF of magnification perturbation, which will be useful for constraining models.

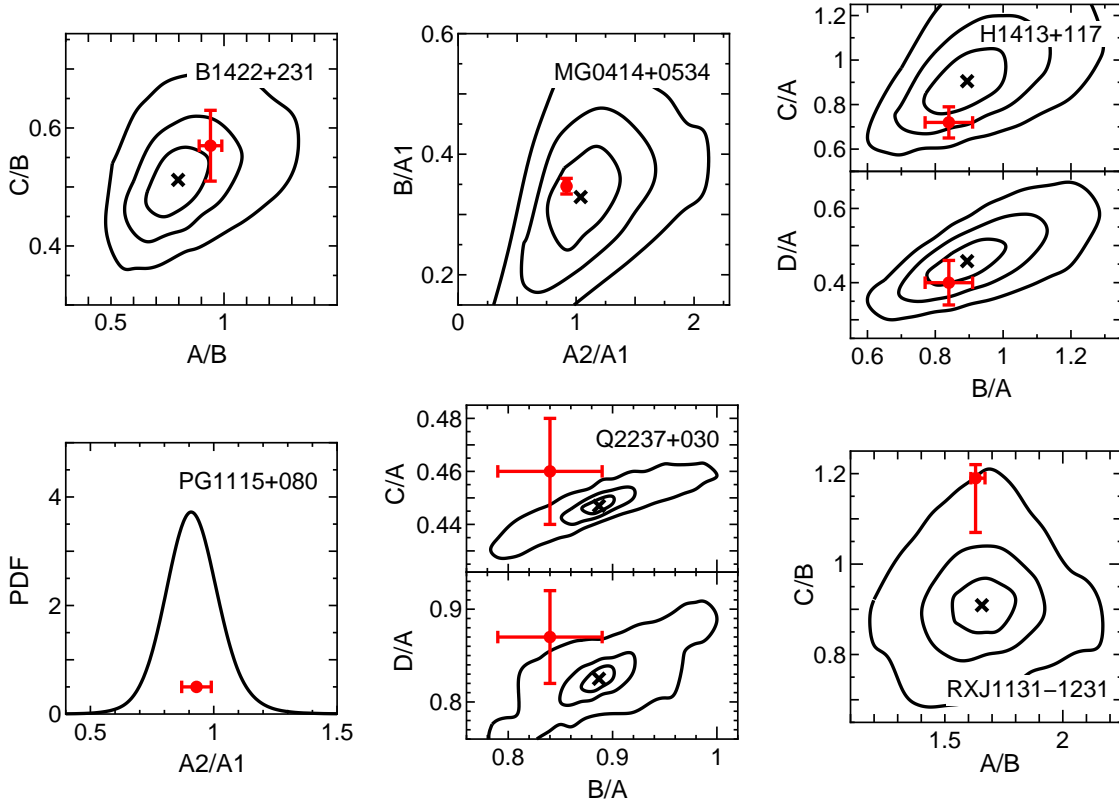


Figure 13. Flux ratios of lensed images for six MIR lens systems. The horizontal and vertical axes are the flux ratios in our simulation except for PG1115+080 where the PDF as a function of the flux ratio $A1/A2$ is plotted, the black crosses show the best-fit values that describe the primary lens models. The black contours around the crosses correspond to 1σ , 2σ , and 3σ confidence regions due to intervening structures, and the red filled circles are the measured results with the 1σ error.

In this work, we have incorporated constraints from astrometric shifts which have been neglected in literature; 1σ errors in the positions of lensed images in optical/NIR observations by HST are used for constraining the possible contribution from line-of-sight structures. However, these values should be considered as upper limits. If we could observe our MIR lenses with better accuracy in the positions, the errors might become smaller. Then, we should observe anomaly in positions of lensed images if we use smooth potential for modeling the primary lenses (Sluse et al. 2012). Therefore, improving accuracy in the positions is necessary for obtaining the lower limits for magnification perturbations. We have considered the effect of reparametrisation of the primary lens model. As we have shown in appendix A, this cannot significantly improve the shift of positions of lensed images. However, it may improve the fit of positions at the order $O(\varepsilon)$. In order to check this effect, we need to perform full Monte-Carlo simulations in which the model parameters are fit together with the perturbations simultaneously. For estimating the magnification perturbation, we have considered two types of filtering, namely “sharp k-space cut” and “constant-shift cut” for filtering perturbations that allow shifts of ε for each image. We have found that the predicted values of magnification perturbation η are consistent

with the numerical results within an error of $\lesssim 30\%$ regardless of types of filtering. In order to filter out perturbations that give the best-fit model more accurately, we need to assess the accuracy of filtering functions more carefully using Monte-Carlo simulations.

In our simulations, we did not include massive line-of-sight haloes which induce large deflection angles ($> 0.0042''$). However, some larger deflection cases may also fit the positions and fluxes by reparametrizing the primary lens. As a result, we emphasize again that our results of magnification perturbations would be a lower limit because it does not include larger deflection cases.

In our simulations, we can resolve halos with a mass of $\sim 10^5 M_\odot$. The corresponding spatial scale is $O[1]$ kpc. However, contribution from much smaller haloes may not be negligible. We expect a boost in magnification perturbations until the size of halo reaches the source size $O[1]$ pc in the MIR band. Therefore, we need to resolve much smaller haloes. N -body simulations with increased number of particles are necessary for accomplishing this purpose.

For simplicity, we did not incorporate baryonic processes such as star formation, gas cooling, radiation feedback in our simulations. Although such baryonic effects may enhance density fluctuations at small scales ($< 1h^{-1}\text{Mpc}$)

(e.g., Jing et al. 2006; van Daalen et al. 2011), we expect that such effects play relatively minor roles in haloes with a mass of $M < 10^7 M_\odot$ since it is difficult to maintain star forming activity in such shallow potential wells. Indeed, the relevant mass scales of intervening structures are equal to or less than $O[10^8] M_\odot$. Therefore, the effect of baryon cooling may be limited except for the central regions of low-mass haloes, though more elaborate analysis should be done to confirm this point.

In order to distinguish between subhalos and the line-of-sight mini-structures (halos or voids), we need to detect the extended source effect (Koopmans 2005; Inoue & Chiba 2005a). Submillimeter imaging of anomalous quadruple lensing with angular resolution of $< 0.1''$ using ALMA will be very useful for measuring the mass and redshift of perturbing objects (Koopmans 2005; Inoue & Chiba 2005b). We will address these issues in future work.

9 ACKNOWLEDGMENTS

We thank Takahiro Nishimichi and Takashi Hamana for kindly providing us the numerical codes. This work was supported in part by JSPS Grant-in-Aid for Scientific Research (B) (No. 25287062) ‘‘Probing the origin of primordial mini-halos via gravitational lensing phenomena’’, and by Hiroaki University Grant for Exploratory Research by Young Scientists. Numerical computations were carried out on SR16000 at YITP in Kyoto University and Cray XT4 at Center for Computational Astrophysics, CfCA, of National Astronomical Observatory of Japan.

APPENDIX A: REPARAMETRISATION OF NEARLY CIRCULAR SIE MODELS

In this appendix, we show that reparametrisation of model parameters of the best-fit SIE model is impossible if a certain position of a lensed image is significantly perturbed while the others remain within the observed errors provided that the eccentricity of the SIE is sufficiently small. For simplicity, we assume that the effective Einstein radius of the best-fit SIE is 1 arcsec and all the 1σ errors of observed positions of lensed images and the centroid of the primary lensing galaxy are equivalent to a constant $\varepsilon \ll 1$ arcsec.

The unperturbed lens equation for the j -th lensed image is then

$$\boldsymbol{\beta} = \boldsymbol{\theta}_j - \boldsymbol{\alpha}(\boldsymbol{\theta}_j; \mathbf{C}), \quad (\text{A1})$$

where \mathbf{C} denotes a set of parameters of an SIE, namely, the angle of the minor axis of elliptic contours of the projected surface mass density θ_e with respect to the horizontal axis, the ellipticity $e \ll 1$, and the effective Einstein radius b' . $\boldsymbol{\beta}, \boldsymbol{\theta}_j$ are the positions of a point source and the best-fit j -th lensed image and $\boldsymbol{\alpha}$ is the reduced deflection angle. All the positions of lensed images $\boldsymbol{\theta}_j$, for $j = 1, 2, 3, 4$ fall within a radius of ε centred at the observed positions $\tilde{\boldsymbol{\theta}}_j$.

Suppose that the j -th lensed image placed at the neighbourhood of a critical curve is significantly perturbed so that the position of the j -th lensed image is shifted from $\boldsymbol{\theta}_j$ to

$\boldsymbol{\theta}_j + \delta\boldsymbol{\theta}_j$ where $\delta\theta_j \gg \varepsilon$ whereas other lensed images are not perturbed. Then the perturbed lensed equation is

$$\boldsymbol{\beta} + \delta\boldsymbol{\beta} = \boldsymbol{\theta}_j + \delta\boldsymbol{\theta}_j - \boldsymbol{\alpha}(\boldsymbol{\theta}_j + \delta\boldsymbol{\theta}_j; \mathbf{C}) - \delta\boldsymbol{\alpha}(\boldsymbol{\theta}_j + \delta\boldsymbol{\theta}_j), \quad (\text{A2})$$

where $\delta\boldsymbol{\beta}$ and $\delta\boldsymbol{\alpha}$ denote the shift of the source due to reparametrisation and the reduced deflection angle with $O(|\delta\boldsymbol{\alpha}(\boldsymbol{\theta}_j)|) \gg \varepsilon$, respectively. In order to fit the observed position $\boldsymbol{\theta}_j$, we reparametrise the parameters \mathbf{C} to $\mathbf{C} + \delta\tilde{\mathbf{C}}$. Then the image position changes by $\delta\tilde{\boldsymbol{\theta}}_j$. Since the lensed images are placed at the neighbourhood of the critical curve, the shift of the source position $\delta\boldsymbol{\beta}$ should be much smaller than $\delta\boldsymbol{\theta}_j$ and $\delta\boldsymbol{\alpha}$. Then, the best-fit reparametrised model should satisfy

$$\left| \frac{\partial\boldsymbol{\alpha}}{\partial\boldsymbol{\theta}_i} \delta\tilde{\boldsymbol{\theta}}_i + \frac{\partial\boldsymbol{\alpha}}{\partial\mathbf{C}} \delta\tilde{\mathbf{C}} \right| \leq \varepsilon, \quad (\text{A3})$$

and the perturbation of positions satisfy $\delta\tilde{\boldsymbol{\theta}}_j \gg \delta\tilde{\boldsymbol{\theta}}_i$ for $i \neq j$. The order of positions are $O(\delta\tilde{\boldsymbol{\theta}}_i) = O(|\delta\tilde{\boldsymbol{\theta}}_i|) = O(\varepsilon)$ for $i \neq j$. We have also

$$\frac{\partial\boldsymbol{\alpha}}{\partial\boldsymbol{\theta}_j} \delta\tilde{\boldsymbol{\theta}}_j + \frac{\partial\boldsymbol{\alpha}}{\partial\mathbf{C}} \delta\tilde{\mathbf{C}} \approx \delta\tilde{\boldsymbol{\theta}}_j. \quad (\text{A4})$$

If the maximum orders of components of $\partial\boldsymbol{\alpha}/\partial\boldsymbol{\theta}_i$ and $\partial\boldsymbol{\alpha}/\partial\mathbf{C}$ are $O(1)$, then we cannot find any reparametrisation that satisfies equation (A3), since we have $O(\delta\tilde{\mathbf{C}}) = O(\delta\tilde{\boldsymbol{\theta}}_j) \gg O(\delta\tilde{\boldsymbol{\theta}}_i) = O(\varepsilon)$.

First, we estimate the order of components of matrices $\partial\boldsymbol{\alpha}/\partial\boldsymbol{\theta}_i$. If the positions of lensed images in circular coordinates are represented as $\boldsymbol{\theta} = (\theta \cos \phi, \theta \sin \phi)$, then the caustic for $b' = 1$ is given by

$$\begin{aligned} \beta_1 &= \frac{\sqrt{q}}{\sqrt{\cos^2 \phi + q^2 \sin^2 \phi}} \cos \phi \\ &- \frac{\sqrt{q}}{\sqrt{1-q^2}} \left[\sinh^{-1} \left(\frac{\sqrt{1-q^2}}{\sqrt{q}} \cos \phi \right) \right] \end{aligned} \quad (\text{A5})$$

$$\begin{aligned} \beta_2 &= \frac{\sqrt{q}}{\sqrt{\cos^2 \phi + q^2 \sin^2 \phi}} \sin \phi \\ &- \frac{\sqrt{q}}{\sqrt{1-q^2}} \left[\sin^{-1} \left(\sqrt{1-q^2} \sin \phi \right) \right], \end{aligned} \quad (\text{A6})$$

where $q = 1 - e$. For $e \ll 1$, equations (A5) and (A6) can be reduced to

$$(\beta_1, \beta_2) \approx \frac{2e}{3} (-\cos^3 \phi, \sin^3 \phi). \quad (\text{A7})$$

Therefore, the width of the asteroid-shaped caustic is $\Delta\beta = \sqrt{2}e/3 \ll 1$. As the source is placed inside the caustic, we have $\beta \approx 0$ and $\boldsymbol{\alpha} \approx \boldsymbol{\theta}_i$. Thus $\partial\boldsymbol{\alpha}/\partial\boldsymbol{\theta}_i \approx \mathbf{1}$ and $O(\partial\boldsymbol{\alpha}/\partial\boldsymbol{\theta}_i) = 1$.

Second, we estimate the order of the components of a matrix $\partial\boldsymbol{\alpha}/\partial\mathbf{C}$, where $\mathbf{C} = (b', e, \theta_e)$. As the reduced deflection angle $\boldsymbol{\alpha}$ is proportional to b' , we have $\partial\boldsymbol{\alpha}/\partial b' \approx \boldsymbol{\theta}_i$. If we assume that the lensed images are sufficiently magnified, then we have $\theta_i \approx 1$ if $b' \approx 1$. Thus $|\partial\boldsymbol{\alpha}/\partial b'| \approx 1$. In a similar manner, we obtain $|\partial\boldsymbol{\alpha}/\partial\theta_e| = |\boldsymbol{\alpha}| = \theta_i \approx 1$. Assuming $e \ll 1$ and $b' \approx 1$, the reduced deflection angle can be approximated as

$$\alpha_1 = \cos \phi - \frac{e(\cos^3 \phi + 3 \cos \phi \sin^2 \phi)}{6} \quad (\text{A8})$$

$$\alpha_2 = \sin \phi - \frac{e(\sin^3 \phi + 3e \sin \phi \cos^2 \phi)}{6}, \quad (\text{A9})$$

where the position of a lensed image is $\boldsymbol{\theta} = (\theta \cos \phi, \theta \sin \phi)$. Therefore, $|\partial\boldsymbol{\alpha}/\partial e| \approx \sqrt{5 - 3 \cos 4\phi}/(6\sqrt{2}) < 1/3$. Thus, we have $O(|\partial\boldsymbol{\alpha}/\partial e|) < 1$ and the maximum order of the components of $\partial\boldsymbol{\alpha}/\partial C$ is 1.

APPENDIX B: TSC SMOOTHING SCHEME

In this appendix, we review the ‘‘Triangular-Shape-Cloud’’ (TSC) scheme in order to calculate a smooth distribution from particles. We derive the window function of the TSC scheme in the Fourier space in two-dimensional systems.

Let us consider the case in which N particles are distributed in a square region. The surface number density of the particles is given by

$$n_0(\mathbf{x}) = \sum_{i=1}^N \delta_D(\mathbf{x} - \mathbf{x}'), \quad (\text{B1})$$

where x_i is the position of i -th particle, and δ_D is the Dirac delta function. The smoothed surface number density is given by the convolution of n_0 and the window function $W(\mathbf{x})$,

$$n(\mathbf{x}) = \int_V d^2\mathbf{x}' n_0(\mathbf{x}') W(\mathbf{x} - \mathbf{x}'), \quad (\text{B2})$$

where $W(\mathbf{x})$ is the window function that specifies the smoothing scheme. The window function of the TSC scheme is

$$W_{\text{TSC}}(\mathbf{x}) = W_{\text{TSC}}(x_1)W_{\text{TSC}}(x_2), \quad (\text{B3})$$

where

$$W_{\text{TSC}}(x) = \frac{1}{r_{\text{grid}}} \begin{cases} 3/4 - (x/r_{\text{grid}})^2, & |x| \leq \frac{r_{\text{grid}}}{2} \\ (3/2 - |x|/r_{\text{grid}})^2/2, & \frac{r_{\text{grid}}}{2} \leq |x| \leq \frac{3r_{\text{grid}}}{2} \\ 0, & \text{otherwise.} \end{cases} \quad (\text{B4})$$

The Fourier transformation is given by

$$W_{\text{TSC}}(\mathbf{k}) = \text{sinc}^3\left(\frac{\pi k_1}{k_{\text{grid}}}\right) \text{sinc}^3\left(\frac{\pi k_2}{k_{\text{grid}}}\right). \quad (\text{B5})$$

As $\text{sinc}^6(x) \approx \exp[-x^2]$ for $|x| \ll 1$, we can approximate the window function by isotropic one

$$W_{\text{TSC}}^2(\mathbf{k}) \approx W_{\text{TSCiso}}^2(k) = \exp(-\pi^2 k^2 / k_{\text{grid}}^2). \quad (\text{B6})$$

For simplicity, we use this isotropic approximated window function instead of the exact anisotropic one. The reason can be explained as follows. As shown in Fig B1, the difference between the original and isotropic one dimensional squared window functions is < 0.02 and the fractional difference is $\lesssim 0.3$ for $x = \pi k / k_{\text{grid}} < 0.5$. The difference becomes conspicuous at $x > 0.5$, which originates from the anisotropy of grids. However, as long as the smoothing scheme is robust, such differences should not affect the result as the differences are limited to the tail part. For instance, in our case, the Poisson noise dominates the signal on very small scales, which correspond to the tail part. Therefore, the tiny error in the tail of the isotropic window function does not affect the result as it is almost masked by the Poisson noise. In terms of $r_{\text{grid}} = 2\pi/k_{\text{grid}}$, the isotropic window function can be also written as

$$W_{\text{TSCiso}}^2(k) = \exp[-k^2 r_{\text{grid}}^2 / 4]. \quad (\text{B7})$$

APPENDIX C: CONSTANT-SHIFT CUT

The use of the constant-shift (CS) cut is verified as follows. The variance of the shift ε of a pair of lensed images separated by an angle θ_{max} is approximately given by a finite sum

$$\langle \varepsilon^2 \rangle = \sum_i \frac{d\langle \varepsilon^2(\theta_{\text{max}}, k_i) \rangle}{d \ln k} \Delta \ln k_i, \quad (\text{C1})$$

where $\Delta \ln k_i$ is a logarithmic interval in the wavenumber k . Although the correlation between different modes is not negligible due to the non-linearity of fluctuations at scales $\lesssim 1$ Mpc, binning of different modes may weaken such a correlation. Suppose a simplest case in which the variance of the shift is approximately given by independent two modes with wavenumbers $k_x, k_y (k_x > k_y)$ and the both modes $\varepsilon(k_x), \varepsilon(k_y)$ obey a Gaussian distribution with variances $\sigma_x, \sigma_y (\sigma_x > \sigma_y)$ as a result of binning. If the variance of the shift $\langle \varepsilon^2 \rangle = \langle \varepsilon^2(k_x) + \varepsilon^2(k_y) \rangle$ is larger than $\varepsilon^2(\text{obs})$, we have to impose a restriction $\varepsilon^2(k_x) + \varepsilon^2(k_y) \leq \varepsilon^2(\text{obs})$ on these modes. In other words, the domain of the input modes should be restricted on a disk with a radius $\varepsilon(\text{obs})$ (see Fig. C1). Consequently, the widths of the constrained PDF are the same except for modes (such as k_y) whose widths of the original PDF are smaller than the radius. Approximating these constrained PDFs by Gaussian PDFs with a fixed variance that corresponds to the size of the radius, one obtains the constant-shift (CS) cut, which makes the power of the shift constant at modest scales $k_{\text{lens}} < k < k_{\text{cut}}$. In a similar manner, one can easily apply these arguments to the cases with many modes. In general, the strong mode-coupling will inhibit our Gaussian approximation. However, the constraint on the shift naturally leads to a selection of modes with small fluctuations. Therefore, we expect that the Gaussian assumption works well even in the strong non-linear regime if the constraints on the positions are stringent enough.

REFERENCES

- Amara A., Metcalf R. B., Cox T. J., Ostriker J. P., 2006, *Monthly Notices of the Royal Astronomical Society*, 367, 1367
- Chen J., 2009, *Astronomy & Astrophysics*, 498, 49
- Chen J., Koushiappas S. M., Zentner A. R., 2011, *Astrophysical Journal*, 741
- Chen J., Kravtsov A. V., Keeton C. R., 2003, *Astrophysical Journal*, 592, 24
- Chiba M., 2002, *The Astrophysical Journal*, 565, 17
- Chiba M., Minezaki T., Kashikawa N., Kataza H., Inoue K. T., 2005, *Astrophysical Journal*, 627, 53
- Coles P., Jones B., 1991, *Monthly Notices of the Royal Astronomical Society*, 248, 1
- Crocce M., Pueblas S., Scoccimarro R., 2006, *Monthly Notices of the Royal Astronomical Society*, 373, 369
- Das S., Ostriker J. P., 2006, *Astrophysical Journal*, 645, 1
- Eisenstein D. J., Hu W., 1999, *Astrophysical Journal*, 511, 5
- Falco E. E., Gorenstein M. V., Shapiro I. I., 1985, *Astrophysical Journal Letter*, 289, L1

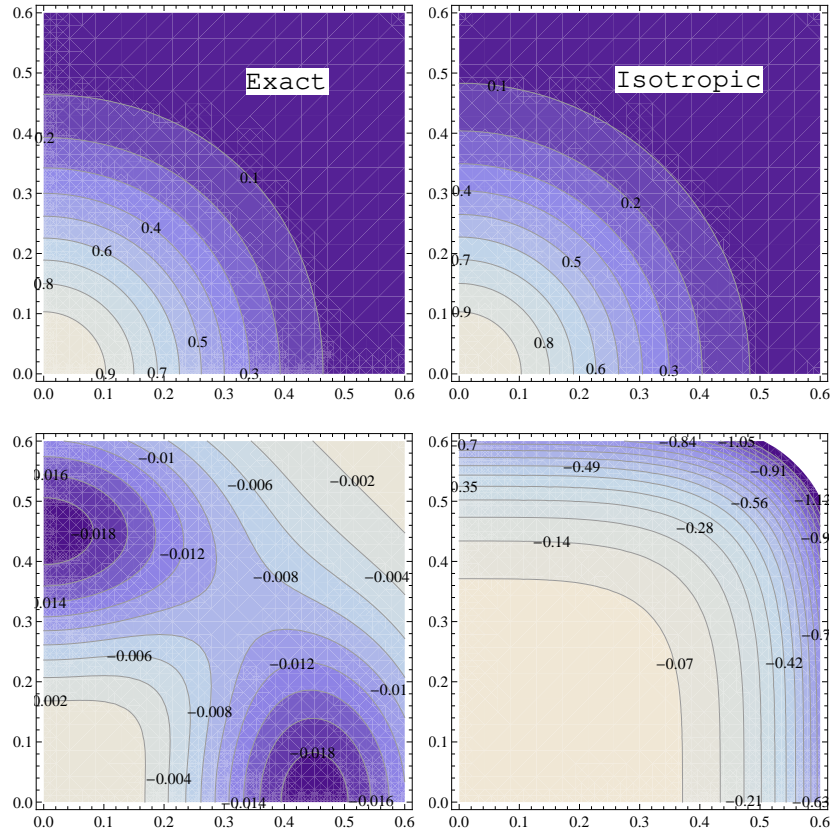


Figure B1. Contour plots of the squared TSC window function $W_{\text{TSC}}^2(\mathbf{k})$ (upper left), its isotropic approximation $W_{\text{TSCiso}}^2(\mathbf{k})$ (upper right), the difference $W_{\text{TSC}}^2(\mathbf{k}) - W_{\text{TSCiso}}^2(\mathbf{k})$ (lower left), and the fractional difference $1 - W_{\text{TSCiso}}^2(\mathbf{k})/W_{\text{TSC}}^2(\mathbf{k})$ (lower right). The wavenumber k is normalized by k_{grid}/π .

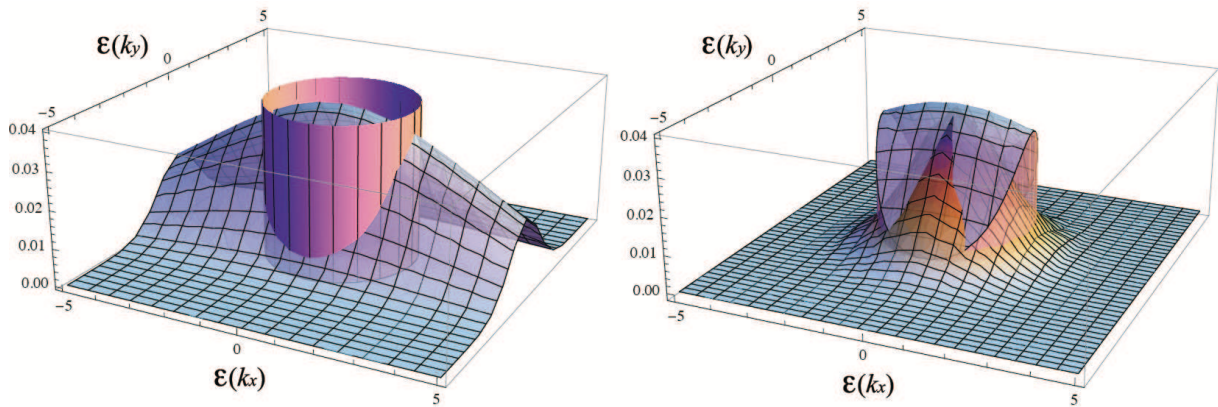


Figure C1. Plots of the original Gaussian PDF (left) and the constrained PDF with its Gaussian approximation (right). The constrained PDF is obtained by imposing a condition $\varepsilon^2(k_x) + \varepsilon^2(k_y) \leq \varepsilon^2(\text{obs})$. Here we assume $\sigma_x = 4$ and $\sigma_y = 1$.

- Goicoechea L. J., Shalyapin V. N., 2010, *Astrophysical Journal*, 708, 995
- Hewitt J. N., Turner E. L., Lawrence C. R., Schneider D. P., Brody J. P., 1992, *Astronomical Journal*, 104, 968
- Hilbert S., White S. D. M., Hartlap J., Schneider P., 2007, *MNRAS*, 382, 121
- Huchra J., Gorenstein M., Kent S., Shapiro I., Smith G., Horine E., Perley R., 1985, *Astronomical Journal*, 90, 691
- Inoue K. T., Chiba M., 2005a, *Astrophysical Journal*, 634, 77
- Inoue K. T., Chiba M., 2005b, *Astrophysical Journal*, 633, 23
- Inoue K. T., Takahashi R., 2012, *MNRAS*, 426, 2978
- Jain B., Seljak U., White S., 2000, *Astrophysical Journal*, 530, 547
- Jarosik N., Bennett C. L., Dunkley J., Gold B., Greason M. R., Halpern M., Hill R. S., Hinshaw G., Kogut A., Komatsu E., Larson D., Limon M., Meyer S. S., Nolte M. R., Odegard N., Page L., Smith K. M., Spergel D. N., Tucker G. S., Weiland J. L., Wollack E., Wright E. L., 2011, *Astrophysical Journal Supplement Series*, 192, 1
- Jing Y. P., Zhang P., Lin W. P., Gao L., Springel V., 2006, *Astrophysical Journal Letter*, 640, L119
- Kayo I., Taruya A., Suto Y., 2001, *Astrophysical Journal*, 561, 22
- Kofman L., Bertschinger E., Gelb J. M., Nusser A., Dekel A., 1994, *Astrophysical Journal*, 420, 44
- Koopmans L. V. E., 2005, *Monthly Notices of Royal Astronomical Society*, 363, 1136
- Kundic T., Hogg D. W., Blandford R. D., Cohen J. G., Lubin L. M., Larkin J. E., 1997, *Astronomical Journal*, 114, 2276
- Lawrence C. R., Elston R., Januzzi B. T., Turner E. L., 1995, *Astronomical Journal*, 110, 2570
- Maccio A. V., Miranda M., 2006, *Monthly Notices of the Royal Astronomical Society*, 368, 599
- McKean J. P., Koopmans L. V. E., Flack C. E., Fassnacht C. D., Thompson D., Matthews K., Blandford R. D., Readhead A. C. S., Soifer B. T., 2007, *Monthly Notices of the Royal Astronomical Society*, 378, 109
- MacLeod C. L., Jones R., Agol E., Kochanek C. S., 2012, *ArXiv:1212.2166*
- MacLeod C. L., Kochanek C. S., Agol E., 2009, *Astrophysical Journal*, 703, 1177
- Magain P., Surdej J., Swings J. P., Borgeest U., Kayser R., Kuhr H., Refsdal S., Remy M., 1988, *Nature*, 334, 325
- Mao S., Schneider P., 1998, *Monthly Notices of the Royal Astronomical Society*, 295, 587
- Metcalf R. B., 2005, *The Astrophysical Journal*, 629, 673
- Metcalf R. B., Madau P., 2001, *The Astrophysical Journal*, 563, 9
- Metcalf R. B., Moustakas L. A., Bunker A. J., Parry I. R., 2004, *Astrophysical Journal*, 607, 43
- Minezaki T., Chiba M., Kashikawa N., Inoue K. T., Kataza H., 2009, *Astrophysical Journal*, 697, 610
- Miranda M., Maccio A. V., 2007, *Monthly Notices of the Royal Astronomical Society*, 382, 1225
- More A., McKean J. P., More S., Porcas R. W., Koopmans L. V. E., Garrett M. A., 2009, *Monthly Notices of the Royal Astronomical Society*, 394, 174
- Nishimichi T., Shirata A., Taruya A., Yahata K., Saito S., Suto Y., Takahashi R., Yoshida N., Matsubara T., Sugiyama N., Kayo I., Jing Y. P., Yoshikawa K., 2009, *Publications of the Astronomical Society of Japan*, 61, 321
- Patnaik A. R., Browne I. W. A., Walsh D., Chaffee F. H., Foltz C. B., 1992, *Monthly Notices of the Royal Astronomical Society*, 259, 1
- Peng C. Y., 2004, PhD thesis, Steward Observatory, University of Arizona
- Riess A. G., Macri L., Casertano S., Sosey M., Lampeitl H., Ferguson H. C., Filippenko A. V., Jha S. W., Li W. D., Chornock R., Sarkar D., 2009, *Astrophysical Journal*, 699, 539
- Ros E., Guirado J. C., Marcaide J. M., Perez-Torres M. A., Falco E. E., Munoz J. A., Alberdi A., Lara L., 2000, *Astronomy and Astrophysics*, 362, 845
- Schechter P. L., Moore C. B., 1993, *Astronomical Journal*, 105, 1
- Schneider P., Kochanek C., Wambsgans J., 2006, *Gravitational Lensing: Strong, Weak and Micro*. Springer-Verlag Berlin Heidelberg New York
- Sluse D., Chantry V., Magain P., Courbin F., Meylan G., 2012, *Astronomy and Astrophysics*, 538, A99
- Sluse D., Kishimoto M., Anguita T., Wucknitz O., Wambsgans J., 2013, *Astronomy & Astrophysics*, 553, A53
- Sluse D., Surdej J., Claeskens J. F., Hutsemekers D., Jean C., Courbin F., Nakos T., Billeres M., Khmil S. V., 2003, *Astronomy and Astrophysics*, 406, L43
- Smith R. E., Peacock J. A., Jenkins A., White S. D. M., Frenk C. S., Pearce F. R., Thomas P. A., Efstathiou G., Couchman H. M. P., 2003, *Monthly Notices of the Royal Astronomical Society*, 341, 1311
- Springel V., 2005, *Monthly Notices of the Royal Astronomical Society*, 364, 1105
- Springel V., Yoshida N., White S. D. M., 2001, *New Astronomy*, 6, 79
- Stalevski M., Jovanović P., Popović L. Č., Baes M., 2012, *Monthly Notices of Royal Astronomical Society*, 425, 1576
- Sugai H., Kawai A., Shimono A., Hattori T., Kosugi G., Kashikawa N., Inoue K. T., Chiba M., 2007, *Astrophysical Journal*, 660, 1016
- Takahashi R., Oguri M., Sato M., Hamana T., 2011, *Astrophysical Journal*, 742, 15
- Takahashi R., Sato M., Nishimichi T., Taruya A., Oguri M., 2012, *Astrophysical Journal*, 761, 152
- Taruya A., Takada M., Hamana T., Kayo I., Futamase T., 2002, *Astrophysical Journal*, 571, 638
- Tonry J. L., 1998, *Astronomical Journal*, 115, 1
- Tonry J. L., Kochanek C. S., 1999, *Astronomical Journal*, 117, 2034
- Trotter C. S., Winn J. N., Hewitt J. N., 2000, *The Astrophysical Journal*, 535, 671
- van Daalen M. P., Schaye J., Booth C. M., Dalla Vecchia C., 2011, *Monthly Notices of Royal Astronomical Society*, 415, 3649
- Weymann R. J., Latham D., Roger J., Angel P., Green R. F., Liebert J. W., Turnshek D. A., Turnshek D. E., Tyson J. A., 1980, *Nature*, 285, 641
- Wong K. C., Keeton C. R., Williams K. A., Momcheva I. G., Zabludoff A. I., 2011, *Astrophysical Journal*, 726
- Xu D., Mao S., Wang J., Springel V., Gao L., White S., Frenk C., Jenkins A., Li G., Navarro J., 2009, *Monthly Notices of the Royal Astronomical Society*, 398, 1235

Xu D. D., Mao S., Cooper A. P., Gao L., Frenk C. S.,
Angulo R. E., Helly J., 2012, *Monthly Notices of the Royal
Astronomical Society*, 421, 2553

Xu D. D., Mao S. D., Cooper A. P., Wang J., Gao L. A.,
Frenk C. S., Springel V., 2010, *Monthly Notices of the
Royal Astronomical Society*, 408, 1721